Universitatea
Transilvania
din Brașov

INTERDISCIPLINARY DOCTORAL SCHOOL

Faculty of Materials Science and Engineering

Edit Roxana MOLDOVAN

Contribution to the laser surface texturing of AISI 430 stainless steel

SUMMARY

Scientific supervisor

Prof.Dr.Eng. Mircea Horia ȚIEREAN

BRAȘOV, 2022

CONTENTS

Introduction

To do a PhD program starts from the ease of outlining around my personality, with a desire to reach the highest possible degree, to be the best. The decision was a natural one, as a continuation of the master's program, but also thank to my coordinating teacher that influenced the passion for research and innovation. The doctorate gives the confirmation of my thinking, of the skills acquired over the years, the release of prejudices and limitations. During the years of PhD study, I have gained main benefits as presentation and public speaking skills, teaching, time management and networking. But the most personal motivation was the fulfilment of researching a subject that you love, with the people you enjoy working.

Acknowledgment

With the completion of the present thesis begin a new stage begins with new opportunities for me. This would not be possible without the persons who helped and supported me, to whom I dedicate the following acknowledgments and gratitude.
The first contentedness is for scientific coordinator Prof.Dr.Eng. Mircea-Horia Țierean, for guiding me during my doctoral studies and which gave me an amazing opportunity by giving full freedom to explore and research the present thesis.
A special gratitude aims the members of the guidance committee, Prof.Dr.Eng. Liana Sanda Baltes, Prof.Dr.Eng. Alexandru Pascu and Prof.Dr.Eng. Cătălin Croitoru for the valuable time granted throughout my doctoral studies.
I express special gratifications to Prof. José Luis Ocaña for bridging people, knowledge, and technology, for all the support granted and truly friendship.
For all the help offered in the realization of the applicative character of the micro texturing with the laser beam, I want to thank Carlos Concheso Doria and BSH Home Appliances Group from Zaragoza.
My thanks are addressing to Associate professor Bogdan Istrate, Prof. Univ. Habil. Dr. Ing. Nicanor Cimpoeșu, for the patience they showed in characterizing the samples by microscopy SEM and EDX spectrometry.
Last but not least, I would like to thank the characterization facilities offered by the Research Institute of Transilvania University.

Notice

This PhD thesis contains information previously published in the papers [74-77]. Paper [77] was presented in May 2022 at ICIR Euroinvent conference, receiving the Best paper award and Best oral presentation award.
The numbers of the figures, tables and bibliographical references in the abstract are those in the thesis.

1. State of art of Laser Surface Texturing (LST)

1.1. What is Laser Surface Texturing?

In Materials Engineering there are different ways to add new functionality to a particular part. The easy case is to change, before the design, the material to a better one, but usually also involves an increase in the complexity of the production process, that increase the product's price. If the using of the parts requires special surface properties, one way is to apply a coating. In this case it is keep the same base material and only in the outer layer is applied another material to ensure the desired properties. In this situation it is necessary to introduce a special step in manufacturing, that still requires expensive investment for implementation. Another way to modify the surface properties is the texturing of the surface, keeping the base material unchanged, but only modifying the microstructure of his surface. **Texturing is a surface functionalisation process, through which the structural architecture and roughness of the surface are changed, in order to give it properties not previously possessed.**

Texturing is not only an artificial functionalization technology, also having few examples of natural microstructures [140]:

- gecko lizard (Lucasium Steindachneri) with hydrophobicity, low sand adhesion, antibacterial and self-cleaning surface [125],
- honeybees' hydrophobic wings that enable flying through fog and dew [64],
- lotus leaf with water-repellent properties that allow them to remain on the water surface if sprayed [15],
- shark's skin having drag reduction and hydrophobic properties, allowing them the rapid swimming [16,135].

Different processes can be used to apply the artificial functionalization by texturing technology:

- ultrasonic grinding [13,16,40,131],
- plasma treatment [57,68,71],
- cutting [127],
- chemical etching [96,106],
- grinding [105],
- roll-imprinting [70],
- interference lithography [97],
- selective laser melting/sintering [49,79],
- laser surface texturing [2,5,8-10,16-26,30,32,35-39,41-48,50,55,57,59-61,63,65,67,74-77,80-85,87-95,100-104,107-110,116,118,120,122,126,129-133,137].

All these factors justify the study of the subject Laser Surface Texturing, with 2926 publications selected from the Web of Science Core Collection in the period 2017-2022 [141]. The structure of the LSP publications in the last 5 years is presented in Figures 1.1-1.3, 36.8% of them being published in Materials Science Multidisciplinary category, 88.17% of them being articles.

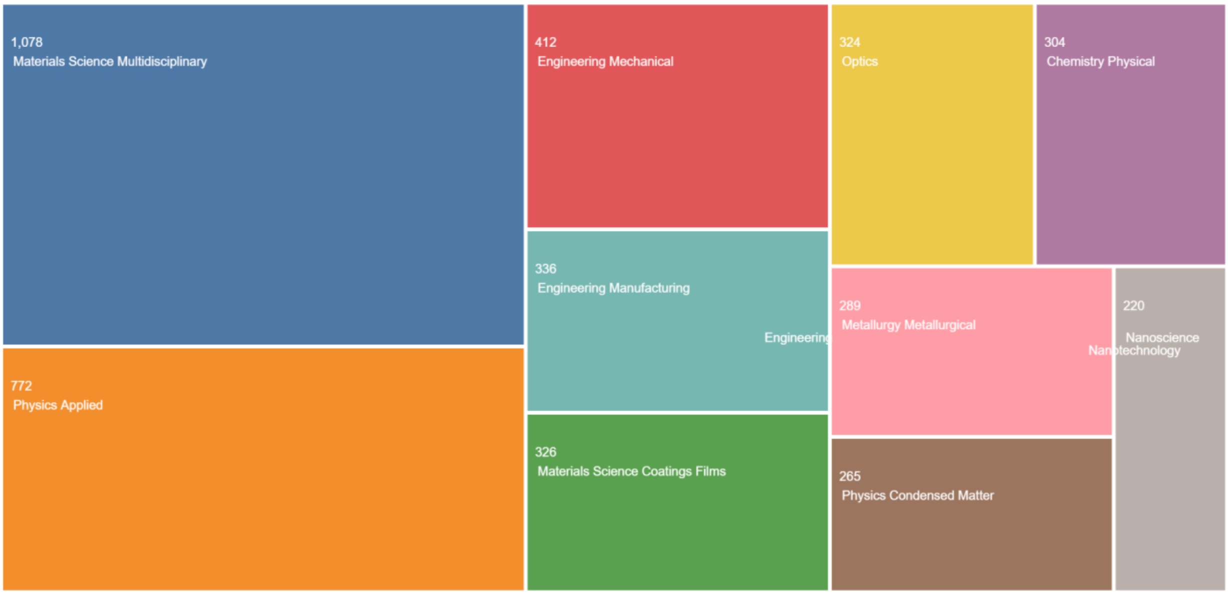

Figure 1.1. Structure of the publications with LST subject selected from the Web of Science Core Collection in the period 2017-2022, by categories [141].

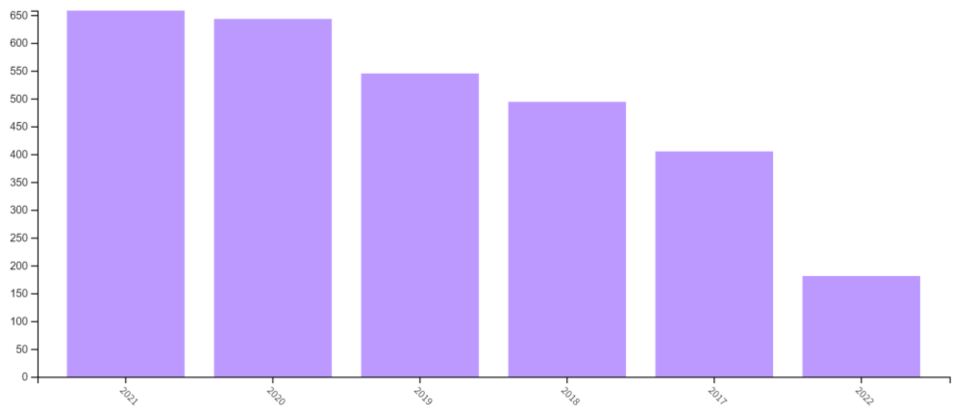

Figure 1.2. Structure of the publications with LST subject selected from the Web of Science Core Collection in the period 2017-2022, by year [141].

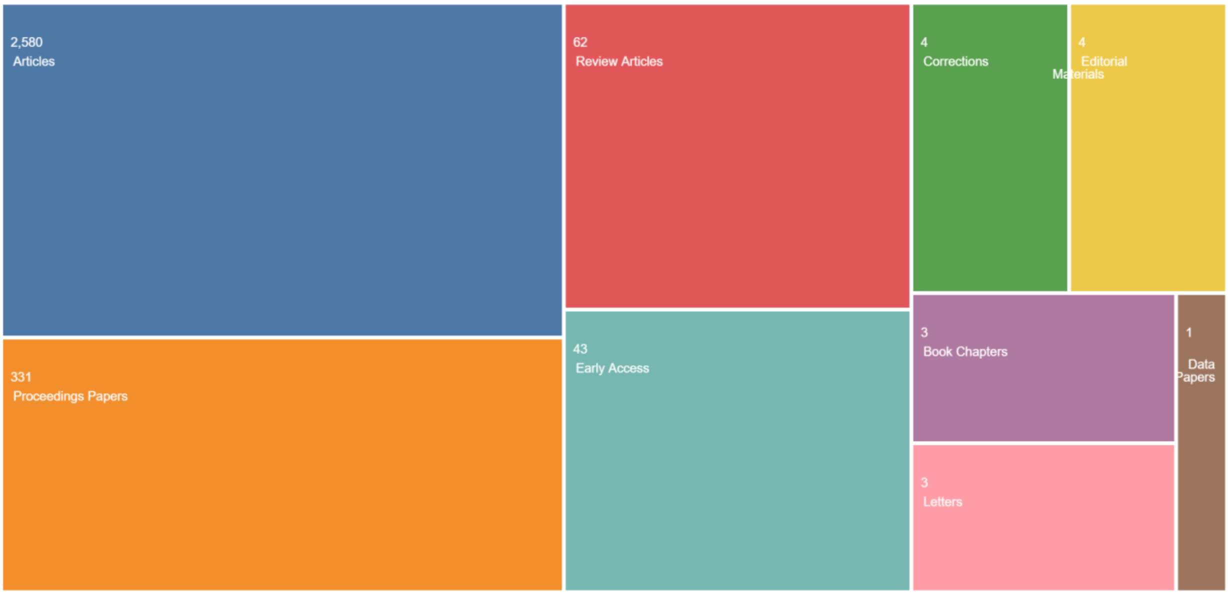

Figure 1.3. Structure of the publications with LST subject selected from the Web of Science Core Collection in the period 2017-2022, by document type [141].

1.2. Types of textures created using laser

Laser surface texturing (LST) is a useful method of generating patterns on the materials surfaces to make microstructures. By LST it can remove material from the surface (by dissolving, evaporating, expelling and/or melting) to modify the surface roughness, increasing the contact area, beneficial for joining.

LST can be implemented on various categories of materials, such as metal (copper, titanium, magnesium, aluminum and their alloys, cobalt-chromium alloys, stainless steel, etc.), polymers (PP, PE, PLLA, PMMA, PEEK, etc.), ceramics (Al_2O_3, ZrO_2, etc.) and composites (PP/fiberglass reinforced aluminum, magnesium/PET alloy, AISI 304/PA6, SiC/SiC, C/SiC, etc.). Usually, the pattern can be regular or irregular, in the form of grooves, dimples, bumps or other patterns [75].

The most used pattern designs [76] were dimple/hole/crater array [26,41,48,55,67,87,120,122,134], parallel lines [2,34,35,39,47,61,65,81,97,104,115,129,137], meshed or cross-pattern [5,39,87,104,108,137]. Outstanding pattern designs were rectangle [120], triangle [120], coral-rock and star-like [49], ellipse [18], concentric circles [78], micropillars [81], Siberian-Cocklebur-like [32].

1.3. Processing parameters for LST

For task-specific applications, laser surface texturing (LST) is a method that allows, in terms of performance, the surface improvement of an engineered material. [75].

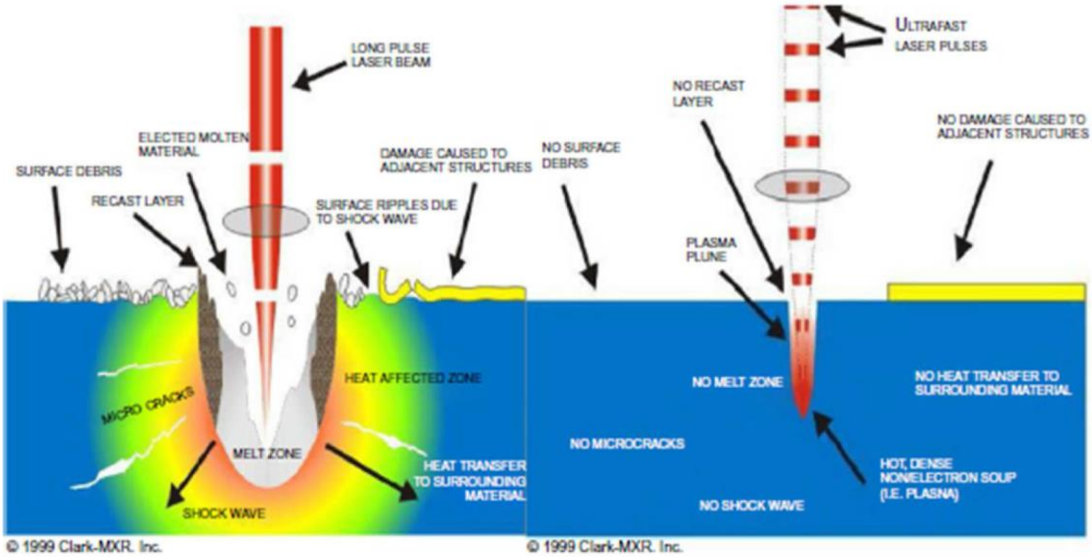

Figure 1.11. Difference between nanosecond pulse laser-material interactions (left) and femtosecond pulse laser-material interactions (right) [23].

To obtain at the same time, the expected texture on the material surface and to reduce the possible defects, it is of major importance to consider the following parameters: intensity of the laser, energy per pulse, laser wavelength, frequency of the laser pulses, polarization, repetition number and rate, focal distance, the angle of incidence, scanning speed, number of cycles, pulse overlapping, number of overlapped scanning layers [23]. De Zanet A. et al. present in [23] the differences between nanosecond and femtosecond pulse laser-material interactions for ceramics (Figure 1.11). The authors concluded that femtosecond-pulsed lasers, are most promising to achieve high-precision textures on ceramics, due of the nearly absent adverse thermal effects near ablated area, [23].

1.4. Applications of LST

Laser surface texturing (LST) is a widely used method worldwide [74-77] for surface functionalization [43,80,85,88], being used in various fields: medical implants [10,19,22,24,42,83,107], wettability tuning [35,39,47,76,100,114], optical properties [95,97], tribological improvements [25,79,91], increasing adhesion [16,57,96], heat exchangers [1], photovoltaics industry [9,44], painting [38], cutting tools [31,112,113,136] and hybrid joining [4,6,7,11,74,79,84,90,92,94,97,102,118,123],

Hybrid joints among distinct materials, such as non-metals (ceramics and polymers) and metals represent a broadly customizable approach used in aerospace [84], automotive industry [6,118], industrial manufacturing [4,11], packing [97], household industries [92], as well as in biomedical [123], aiming lightweight structures that are optimized in terms of production costs and strength [84,90,102]. Microstructuring can be used as pre-treatment in laser processing, before joining dissimilar materials, to achieve a better mechanical interlocking [11,94], to control the physical, chemical and mechanical properties of hybrid joints [7].

1.5. Conclusions

Through processes used to functionalize surface of the materials is Laser Surface Texturing, because is a useful method that can be easily implemented. Laser surface texturing can be applied to on various types of materials by different lasers equipment, using from picosecond, femtosecond or nanosecond laser sources or combinations of lasers, being sought the same results, in terms of improving roughness, wettability and properties of the material surface. According to the laser source and tuning the processing parameters, different shapes and dimension of the microstructures can be obtained.

The most used laser equipment are nanosecond pulsed, conditioned on the part of economic view, and on the other hand by industrial requirements, even if the femtosecond, picosecond lasers equipment are promising to achieve a higher precision, due to nearly absent adverse thermal effects near ablated area. Nanosecond laser source favours melting processes, the resulting structures being dominated by molten and resolidified material and usually larger by an order of magnitude than femtosecond laser microstructuring.

Applications of surface texturing is wide, but LST with a nanosecond pulsed laser can be founded in tribological applications, improving corrosion resistance, hybrid joining (metal-polymer), to reveal hydrophobic/super hydrophobic behaviour, biomedical materials and applications (improve osteoblastic bond of human stem cells, implantation of stem cells in biopolymers, dentistry and orthodontics.

2. Objectives of the Thesis

Analysing the conclusions of the previous chapter and industrial requirements, the objectives of the present research are:

- Making laser surface textures using a cheap industrial nanosecond pulsed laser to apply the results directly to industry. This objective was proposed by the industrial partner, in order to satisfy his future projects, related to the improvement of the products and the cheapening of the technological process.

- Microstructuring of closed loop grooves, resulted from the study of the scientific literature and the practical internship at the industrial partner. The problem of closed contours is the coincidence between the ending and the starting point, especially in the case of repeated passes.

- Determining the influence of LST design and processing parameters on surface architecture, roughness and wetting behaviour. As some of the textured models, in particular the dimple/hole/crater array, present difficulties in terms of morphological analysis, there are defined the characteristics in terms of morphological analysis to ensure reliable results.

- Providing recommendations for industrial companies that intend to implement this process in production and for designers who wish to propose medical implants, household appliances and cutting tools. By choosing the right pattern and processing parameters can be obtained surface roughness tailoring, wettability tuning, hybrid joining, changing optical properties and increasing adhesion.

The major requirement, in terms of surface functionalization through the LST process, is the accumulation of all possible benefits with a single process, low cost and high process speed.

3. Materials and methods

3.1. Materials

The material selected for Laser Surface Texturing (LST) is a ferritic stainless steel (AISI 430, EN 1.4016, equivalent with X6Cr17, ISO/TS 15510:2003), provided by Acerinox company from Madrid, Spain under the name ACX 500. This grade 430 ferritic stainless steel as the base alloy of the ferritic group, is conveniently available in coil and sheet (up to 1.2 mm thick) most usually in 2B (moderately reflective) or BA (bright annealed) finishes.

Table 3.1. Chemical composition, mechanical and physical properties of AISI 430 stainless steel, according to ASTM A-240 and EN 10088-2:2005.

Classes of properties	**Chemical element**		**Concentration (%)**
Chemical composition	Carbon		≤ 0.080
	Manganese		≤ 1.00
	Silicon		≤ 1.00
	Sulphur		≤ 0.015
	Phosphorous		≤ 0.040
	Chromium		16.00-18.00
	Nitrogen		≤ 0.045
	Properties		**Unit measure**
Mechanical properties	Tensile strength		450-600 MPa
	Proof stress 0.2%		min. 260 MPa
	Elongation		min. 22%
	Hardness max.		89 HRB
Physical properties	Modulus of elasticity	tension	200 GPa
		torsion	65 GPa
	Density		7800 kg/m^3
	Melting point range		1425-1510°C
	Thermal expansion		10.4x10^{-6} /K
	Specific heat capacity		460 J/kgK
	Thermal conductivity	at 100°C	26.1 W/mK
		at 500°C	26.3 W/mK
	Electrical resistivity		600 ηŷm
	Mean coefficient of thermal expansion	0 - 100°C	10.4 μm/mK
		0 - 315°C	11.0 μm/mK
		0 - 540°C	11.4 μm/mK
		0 - 700°C	12.1 μm/mK
	Relative permeability		Ferromagnetic

Because of the surface finish (BA quality), the AISI 430 samples are highly reflective, before enforcing any work onto the foreground of the ferritic stainless steel, an analysis of spectral reflectivity was done. A GTF spectrophotometer (Photonic Technologies Group, Woking, UK) was used to analyse the spectral reflectivity of the material sample before applying the LST.

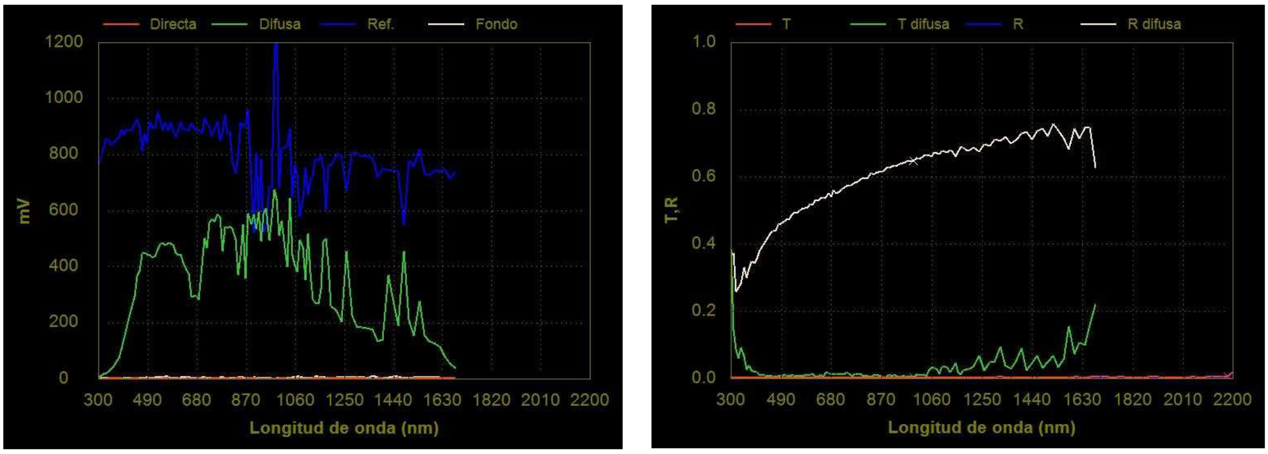

(a) (b)

Figure 3.3. (a) Spectrophotometer calibration spectrum; (b) spectrophotometer of AISI 430 ferritic stainless steel.

Spectral reflectance (Figure 3.4.) indicates the quantity of the incident laser radiation, what is reflected and what is absorbed, by the surface of the material analysed. The spectrophotometric analysis offers the possibility to save the measurement results (thus resulting in the Figure 3.3.b-capture of the screen of the processing equipment), showing the same trend for the results, obtained in terms of the chart analysis of stainless steel (Figure 3.4.).

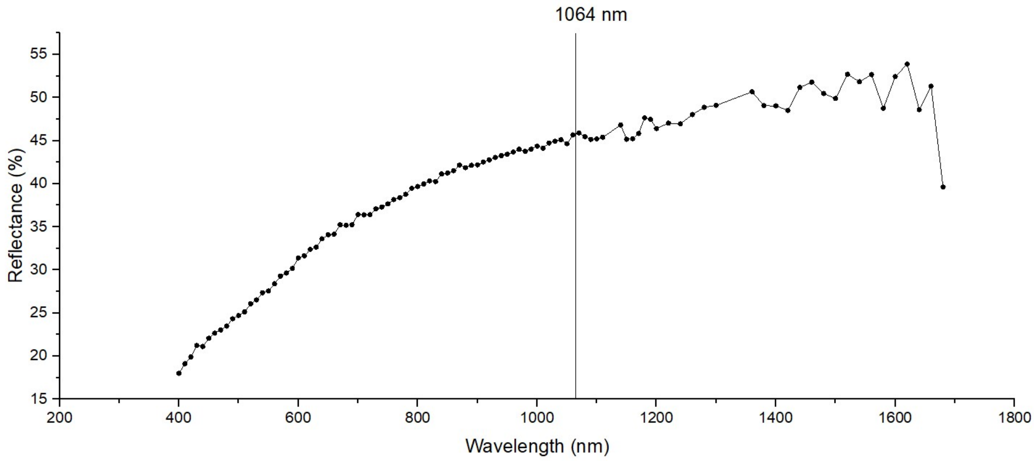

Figure 3.4. Spectral reflectance of sample AISI 430 ferritic stainless steel and wavelength of TruMark 5020 source.

3.2. Processes

3.2.1. Surface micro texturing technology and equipment

Due to integrated PC-aided design software (AutoCAD), integrated in the laser equipment, a large variety of designs can be carried out. To new patterns design this study addresses e.g., 3x concentric octagonal donuts (design type A), two ellipses at an angle of 45° overlapping with its mirror (design type B) and dimple/hole/crater array (design type C). Samples were cut from a large sheet with the dimensions of 80 x 25 x 0.5 [mm]. Previous to laser processing, the samples have been cleaned with

Isopropanol (solution 2-Propanol, with 60 g/mol, molecular weight) for cleaning and degreasing the samples.

Table 3.2. Schematic representation of the patterns design types selected for microtexturing.

	Pattern design	**Sketch detail**
Design type A	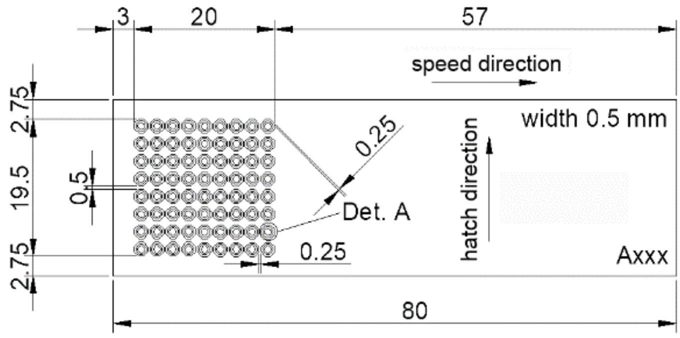	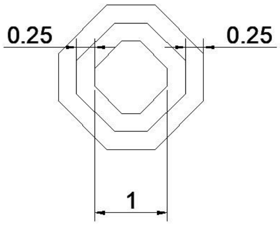
Design type B	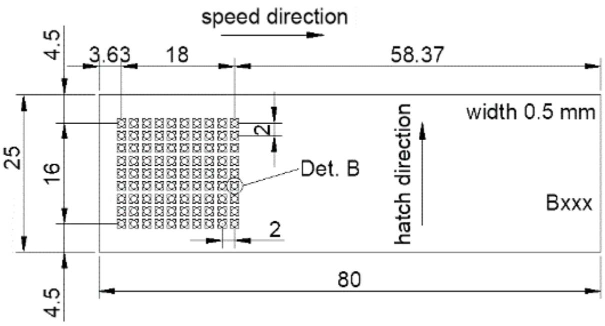	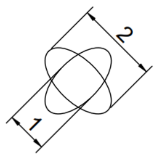
Design type C	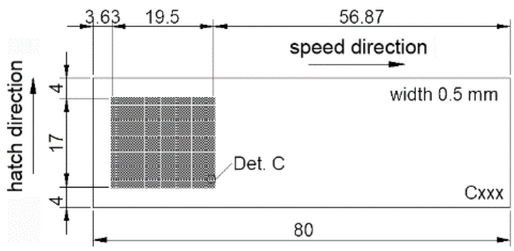	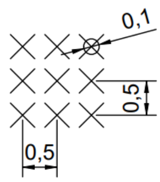

An edge distance was considered, in order to be allowed the use of clamping tools in joining dissimilar materials and, because it's not recommended to create a welding beam on the edge of the ferritic stainless steel because of the fragile predisposition characteristics in the thermally influenced area.

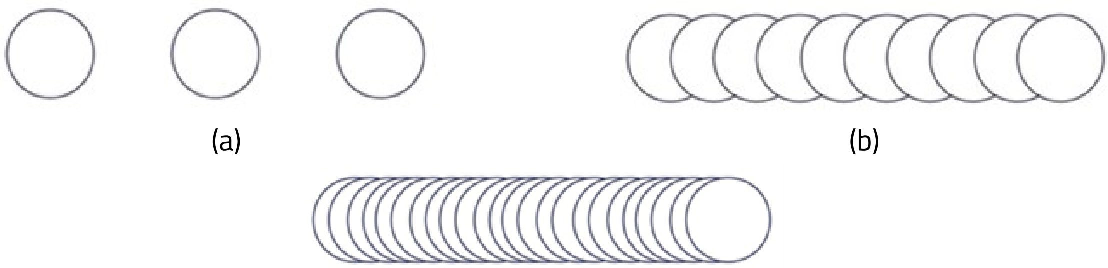

Figure 3.5. Representation of laser spot overlapping 0 % (a), 50% (b) and 90% (c).

Spot overlapping is another important aspect in LST (Figure 3.5). It was observed that overlapping > 90 % will behave and form a continuous dent, like a seam weld. For this reason, is imposed the distance between the laser spot centers of 10 μm (just in the case of design type A and B), resulted from the ratio of speed to frequency. For design type C (with no overlapping) the distance of the laser spot centers is 500 μm. The heat generated via the laser must diffuse efficaciously, while the heat captured in the influenced area must lead to a higher depth while the affected area must be lowered.

The micro texturing was achieved with the help of nanosecond pulsed laser TruMark 5020 (Trumpf Laser und Systemtechnik GmbH, Ditzingen, Germany) equipment, regularly used for marking in industry. Throughout the experiments, the constant parameters were: impulse per point, the laser power, spot diameter, focal distance, power density and the variable parameters were: speed, repetition rate (frequency), number of repetitions, pulse width, presented in Table 3.4. Repeatability was setup, from 1 repetition, up to a maximum of 20 repetitions, for octagonal and ellipse patterns, and maximum 15 repetitions for dimple/hole/crater array pattern. The maximum range of repetitions was selected after observing the intensity of the splashes and burrs. Growing the amount of expulsed material will grow the heat affected area and the recast material.

Table 3.3. Laser marking system TruMark 5020, Trumpf [144].

Property		**Value**
Active medium		Nd: Fiber Diode-pumped
Diameter of rotary table		600 mm
Travel length	Z - axis	265 mm
	Z - axis	1 m/min
	A - axis	22.5 rpm
Wavelength		1064 nm
Average power		≤ 20 W
Power consumption		< 0.6 kW
Beam quality		M^2 ~ 2
Min. diameter in the focal distance		~ 110 μm
Marking area		180 x 180 mm
Focal distance		254 mm
Pulse frequency		5 – 1000 kHz
Pulse duration		9-200 ns
Spot diameter		100 μm (Focal distance=254 mm)

The laser density profile was investigated prior the laser processing to ensure that proper laser absorption into material will be obtained. The intensity distribution profile (Figure 3.7.) of the laser radiation on the surface plane can be described as Gaussian, which provide an image on the future groove's shape. During the laser beam - surface interactions, a high intensity plasma surrounded by an electron charged field is formed which leads to material melting - recasting phenomena and even, to delamination of the surface layer. The Figure 3.8. shows an almost perfect outcome for laser beam, perfect beam and real beam are almost identical.

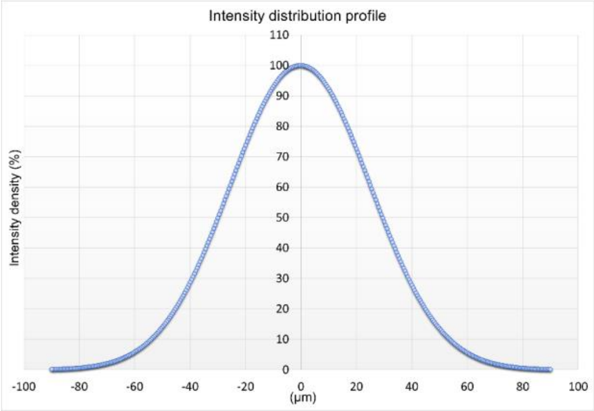

Figure 3.7. Intensity distribution profile of laser beam and range spot for TruMark 5020 equipment.

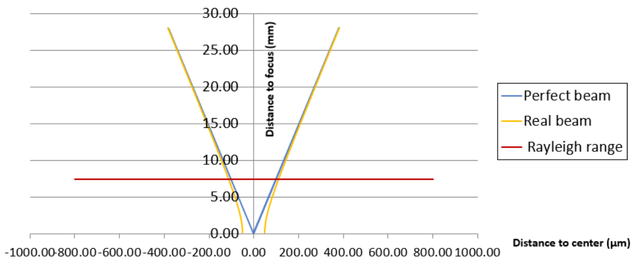

Figure 3.8. Beam simulation of TruMark 5020 laser equipment.

Considering the economic demands in industrial applications, the equipment for laser surface texturing had requirements for an easy automation and high flow rate, setting up the use of a nanosecond pulsed laser in the detriment of the picosecond or femtosecond laser. To gain a 99% overlap, it is essential to maintain a frequency-velocity relationship (relation 3.1 [99]), where the speed is direct proportional to frequency:

$$S = \frac{\left(1-\frac{Os}{100}\right)d\cdot f}{1-\left(1-\frac{Os}{100}\right)w\cdot f} \tag{3.1}$$

where: S = speed [mm/min], Os = overlap of the spot, d = spot diameter [mm], f = frequency [Hz], w = pulse width [ms].

Table 3.4. Constant and variable parameters for applied laser surface texturing pattern on AISI 430 stainless steel.

Constant parameters	Unit measure	Value
Power	[W]	20
Spot diameter	[µm]	100
Power density	[W/cm²]	2.55×10^5
Impulses per point	[number]	1
Track width of the spot	[mm]	0.5
Overlap of the spot	[%]	99
Defocus	[mm]	0
Hatch	[mm]	2.25 (design type A) 2 (design type B) 0.5 (design type C)
Focal distance	[mm]	254
Variable parameters		
Frequency	[kHz]	30-100
Speed	[mm/s]	300-1000
Pulse width	[ns]	170-50
No. of repetitions	[number]	1/5/10/15/20

The number of spots implemented has to assure the successful quality of micro texturing. An important segment was to acquire a great repeatability, due to the identical trajectory for the speed and frequency used. Repeatability changed into selected randomly, begin with one pass, then each 5 repetitions up to a maximum of 20 repetitions (design type A and B) and 15 repetitions (design type C). The highest number of repetitions was selected due to the growth of the splashes and burrs. Increasing the quantity of expulsed material will increase the influenced heat affected area and quantity of the recast material.

Different ranges of parameters (number of repetitions, speed, frequency) have been carried out, but have been hold correlated. Among the results, can be distinguished the evolution of the fluence (ratio of laser pulse energy and surface area), pulse width (time measured at pulse full width half maximum), and pulse energy (Figure 3.9.a.). A pulse energy higher than 400 μJ (frequency from 30 to 50 kHz) occurs at 20 W constant mean power, with 3.8 kW pulsed peak power. For the variety of frequency range used (30–100 kHz), fluence decreases in the 8.49 to 2.55 J/cm^2 domain. This emphasizes a decreasing path for the ablation rate with the increasing of frequency, which means less material is removed from the surface of the micro textured material whilst the frequency increases.

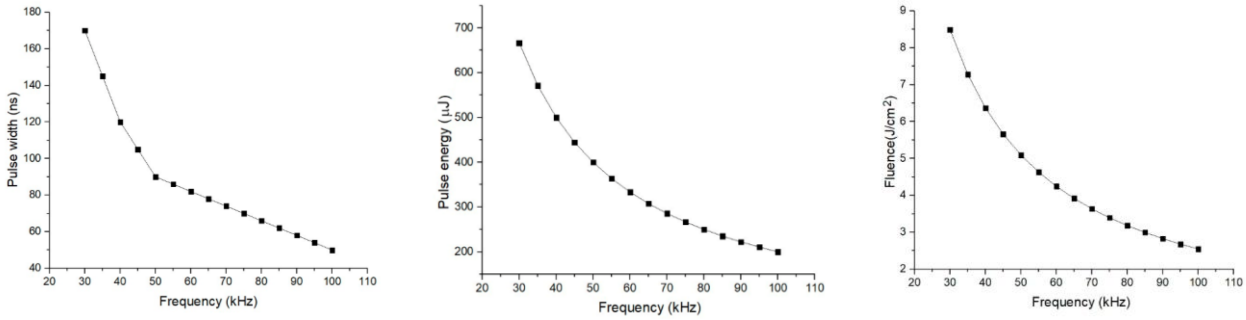

(a) (b) (c)

Figure 3.9. Pulse width (a), pulse energy (b) and fluence (c) engendered by frequency.

The time cycle refers to a single sequence of repetition, decreasing with increasing frequency (Figure 3.10.). The time cycle is an important parameter, as it can indicate the time required to perform micro-texturing. The importance comes from the influence on the capacity and volume of production that can be achieved, thus being able to influence the automation of the LST process.

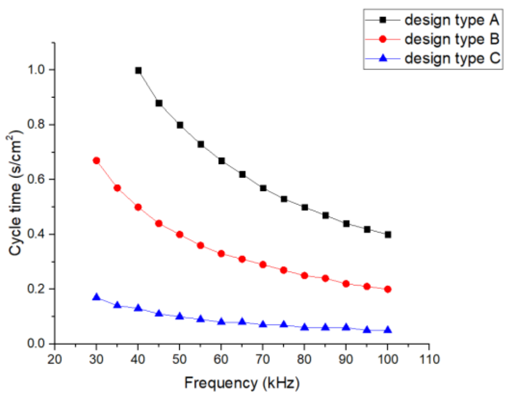

Figure 3.10. Cycle time depending on frequency.

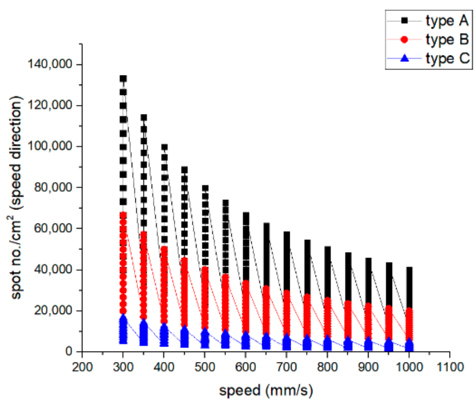

Figure 3.11. Spots density on speed direction

Figure 3.11. represented the spots number per cm^2 by means of speed axis. The speed direction is the course of direct laser texturing process, and the hatch direction is the space among the center to center of the micro texture pattern applied. The spots number may render a decisive factor for defining the essential resolution and for the desired purpose in micro texturing. The range of spots on the hatch path is constant, different for each type of pattern. In the case of speed direction, the variety for the spots numbers is reduced while the speed increases.

3.2.3. Samples preparation

The cutting of stainless steel AISI 430 ferritic has been performed with the help of Struers Accutom 505 equipment, using an abrasive disc Corundum Cut-off wheel (arbor size 12,7 mm). After cutting the micro textured samples, an encapsulation in epoxy resin was prepared using a polyester resin (from Gilca, Zaragoza, Spain) and hardener (MEK peroxide-Ketanox, from Gilca, Zaragoza, Spain).

After the polishing procedure, to develop the microstructure and grains, was used as chemical etchant (Vilella – specific reagent for metallographic analysis on ferritic stainless steel and stainless steel products). The composition of the chemical etchant is 45 ml Glycerol, 30 ml Hydrochloric Acid and 15 ml Nitric Acid. The etching time recommended is 10 seconds. The interruption of etching is by placing the sample under running water and tamponade with a clean cotton material until it dries.

3.3. Characterization techniques and equipment

3.3.1. Morphological analysis

The microscope analysis for top view images 2D and 3D topographic images was performed with an optical microscope upright Olympus BX35 (Olympus Europa Holding GMBH, Germany) and the images have been captured with the help of the camera acquisition Olympus DP73 and a halogen lamp power supply unit Olympus TH4 for brightness control. The images were aquired with the help of a multiport mount adapter and transmitted through a HDMI cable to PC. The program software used was Olympus Stream Motion. The microscope analysis for sectional images and measurements was performed with an optical microscope high-quality phase contrast Leica (Leica Microsystems, Switzerland, Ltd, model DMIL M LED). The images were captured with the help of a camera acquisition integrated in the equipment (Leica Microsystems CH-9435 Heerbrugg, Singapore), a compact illumination unit precentered light emitting diode (LH 113 LED, 12V, Germany) and software Leica Application Suite version 4.10.0.

The microstructuring is performed due to the laser beam local ablation of the material, generating grooves with a certain depth and width, as a function of the operational parameters. Also, near the groove, a part of the ablated material can be deposited as recast material dimples (Figure 3.19). For each sample was measured the height of the recast material (deposited at the edges of the hollow), the width of the crevasse, depth and area of the hollow.

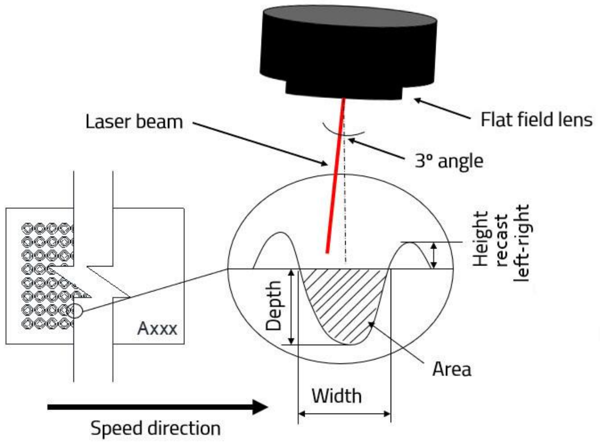

Figure 3.19. Geometry charcaterization (height, width, depth and area) of microstructures on ferritic stainless steel AISI 430.

3.3.2. SEM+EDX analysis

The surface morphology of the samples was investigated by scanning electron microscopy (SEM FEI Quanta 200 3D Dual beam, equipped with energy-dispersive X-ray spectroscopy analysis unit-X flash Bruker, USA). The working distance is set-up at 15 mm in low vacuum mode, with a spot size 5, high voltage (20kV) and detector LFD (Large Field Detector).

3.3.3. Roughness analysis

The equipment selected for the high accuracy measurement of surface roughness is the roughness tester type ISR-C100 (Insize Co, Suzhou New District, China). The measured parameters of surface roughness were: R_a, R_z, and R_t [138,139], according to EN ISO 4287 and EN ISO 16610-21. The measuring and data collecting was done by using the PreSurf 1.0 (Presurf Enterprise) software program.

3.3.4. Wettability analysis

The testing method is known as 'static' or even 'sessile drop', since on many surfaces the droplet remains static and in equilibrium with the material surface and air, according to ISO/TS 14778:2021. When the liquid droplet spreads (is wetted a large area of the surface) means that the static contact angle (SCA) is lower than 90°, resulting a hydrophilic surface. When the angle is higher than 90 degrees, the surface is considered hydrophobic or super hydrophobic. The purpose of the wettability analysis is to observe whether the micro textured surface has a low surface energy and unitary structures. The droplets of the distilled water that were placed on the laser micro textured surfaces with the micropipette to determine the contact angle analyses have a volume of 10 µL. For better accuracy, the procedure was repeated for three times, each micro textured sample and the result are the average of the measurements. While measuring the static contact angle of the laser micro textured surface of the ferritic stainless steel, the video length duration was set for 15 s. The frame was set-up for every second. That means, the results are for the average static contact angle of the measurement for every 15 frames. The equipment used for wettability testing was Ossila CA Goniometer.

4. Morphological analysis of Laser Surface Structuring of AISI 430 Stainless Steel

4.1. Optical microscopy

The top optical micrographs were used to verify the quality on texturing. The cross-section optical micrographs were used to measure the height of the recast material deposited on/near the groove edges (where applicable), width, depth, and area of the groove. The results are the average of five measurements (minimum) of different hollows on the same sample. All the measurements are according to Figure 3.19.

4.1.1. Design type A, octagonal donuts pattern

In the Figure 4.1. are presented image detail of the micro texture, microscopic images, 3D topographic map and cross-section optical micrograph of the sample A (speed 300 mm/s, frequency 30 kHz, no. of repetition 1, pulse duration 170 ns). The measurements with optical microscope on the cross-section images achieved are: average area of 227.17 μm^2, with 7.02 μm depth and 47.73 μm width. The recast material on the left side has an area of 79.13 μm^{2}with 5.23 μm height. The right side has an area of 74.09 μm^2 and 5.99 μm height.

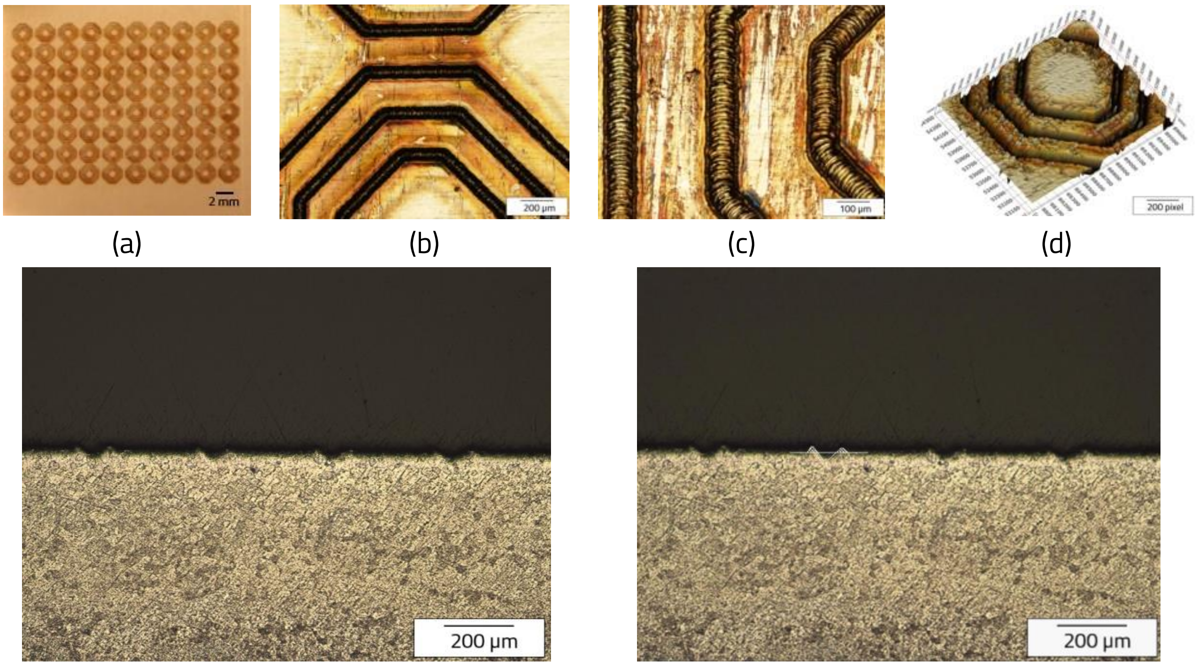

Figure 4.1. Image detail (a), microscopic images (b, c), 3D topographic image (d) and cross-section view (e) of LST design type A, (f) measurements, frequency 30 kHz, speed 300 mm/s, no. of repetition 1.

In the Figure 4.2. is presented the image detail of the micro texture applied, microscopic images and cross-section optical micrograph of the sample A (speed 300 mm/s, frequency 30 kHz, no. of repetition 5, pulse duration 170 ns). The measurements with the optical microscope on the cross-section images achieved offers an average area of 334.58 μm^2, with 9.98 μm depth and 48.70 μm width. The recast material on the left side has an area of 71.01 μm^2 with 5.59 μm height. The right side has an area of 39.13μm^2 and 3.28 μm height.

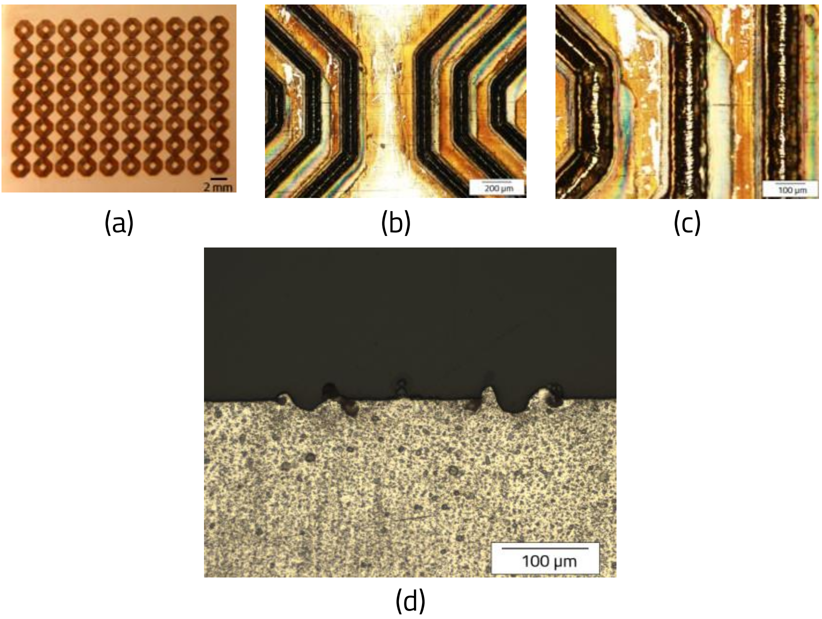

Figure 4.2. Image detail (a), microscopic images (b, c) and cross-section view (d) of LST design type A, frequency 30 kHz, speed 300 mm/s, no. of repetition 5.

When the number of repetitions increases up to 10, can be outlined how thermally area increases, too, up to half the distance between the center of micro patterns. In Figure 4.3.c. a green area appears, which appears to be chromium oxide. In Figure 4.3.d., microscopic cross-section view, the direction of the tilt angle (3°) of the laser beam can be distinguished. One of the edge hollow sides has more recast material.

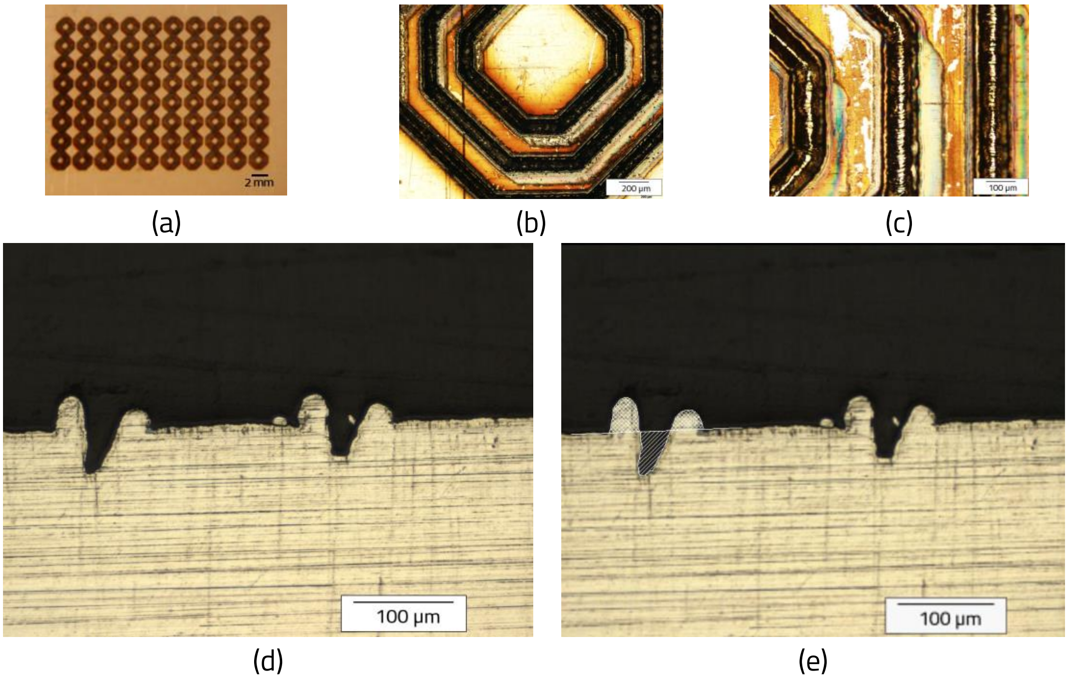

Figure 4.3. Image detail (a), microscopic images (b, c) and cross-section view (d) of LST design type A, (e) measurements, frequency 30 kHz, speed 300 mm/s, no. of repetition 10.

In the Figure 4.4. is presented the sample A (speed 300 mm/s, frequency 30 kHz, no. of repetition 15, pulse duration 170 ns). The measurements with the optical microscope on the cross-section images achieved offers an average area of 499.06 μm^2, with 19.53 μm depth and 40.29 μm width. The recast material on the left side has an area of 75.57 μm^2 with 5.526 μm height. The right side has an area of 187.73 μm^2 and 9.12 μm height.

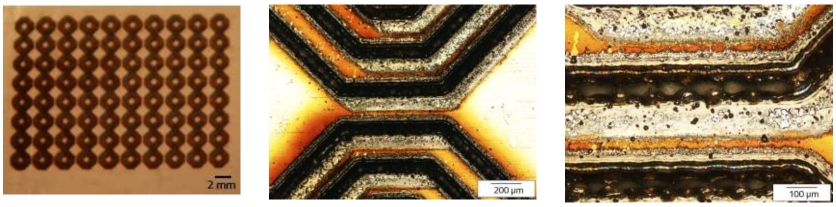

(a) (b) (c)

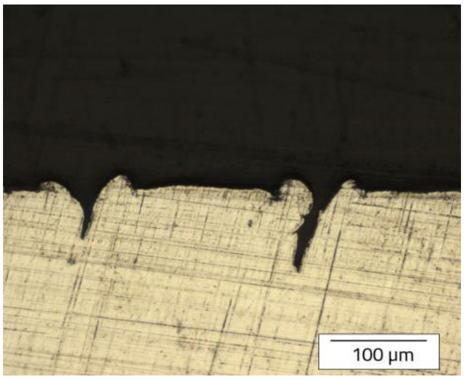

(d)

Figure 4.4. Image detail (a), microscopic images (b, c) and cross-section view (d) of LST design type A, frequency 30 kHz, speed 300 mm/s, no. of repetition 15.

In the Figure 4.5. is presented the sample A (speed 300 mm/s, frequency 30 kHz, no. of repetition 20, pulse duration 170 ns). The measurements with the optical microscope on the cross-section images achieved offers an average area of 379.43 μm^2, with 13.46 μm depth and 43.65 μm width. The recast material on the left side has an area of 158.18 μm^2 with 11.63 μm height. The right side has an area of 138.28 μm^2 and 8.20 μm height.

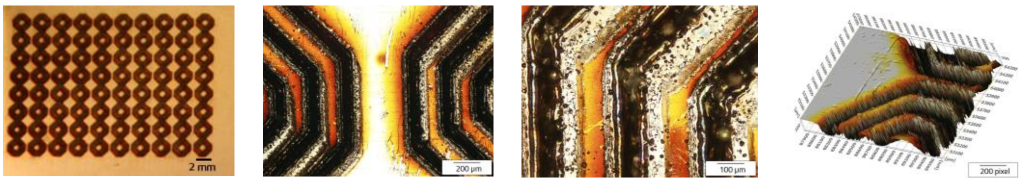

(a) (b) (c) (d)

Figure 4.5. Image detail (a), microscopic images (b, c) and 3D topographic image of LST design type A, frequency 30 kHz, speed 300 mm/s, no. of repetition 20.

While increasing the speed and frequency, can be barely seen a micro texture on image detail of the sample. The microscopic images offer information regarding HAZ, which is almost completely missing, splashes, which are missing and about the slight irregularity of micro texture regarding linearity.

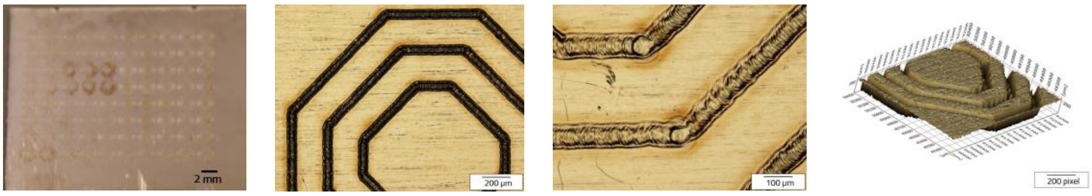

(a) (b) (c) (d)

Figure 4.13. Image detail (a), microscopic images (b, c) and 3D topographic image of LST design type A, frequency 50 kHz, speed 500 mm/s, no. of repetition 1.

When the repetitions number increases to 20, compared to a repetition, a totally different overall picture can be distinguished with the evidence of a well-defined thermally affected area.

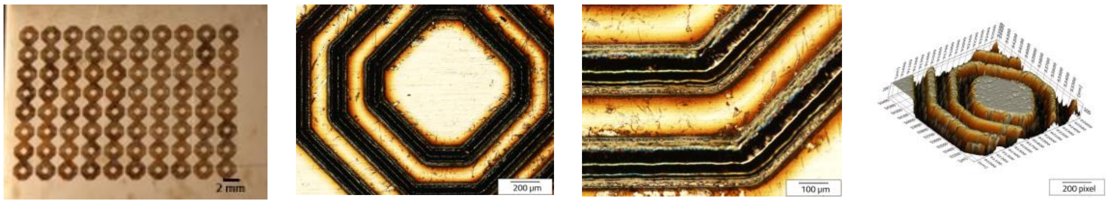

(a) (b) (c) (d)

Figure 4.14. Image detail (a), microscopic images (b, c) and 3D topographic image of LST design type A, frequency 50 kHz, speed 500 mm/s, no. of repetition 20.

According to Figure 4.23 the area and depth of the microstructure increases until 15 repetitions of microstructuring. With the increase in repetition, the recast material elevation increases as well. Also, inversely proportional to the number of repetitions, the width of the groove tends to decrease. This tendency occurs because in the case of increased repetition the expelled material can no longer reach the surface of the workpiece as recast material, and instead will be deposited on the walls of the hollow narrowing the width of the groove. The deposited recast material is influenced by the laser beam angle alignment, resulting in one part of the recast material to be larger than the other side, depending on the laser beam direction.

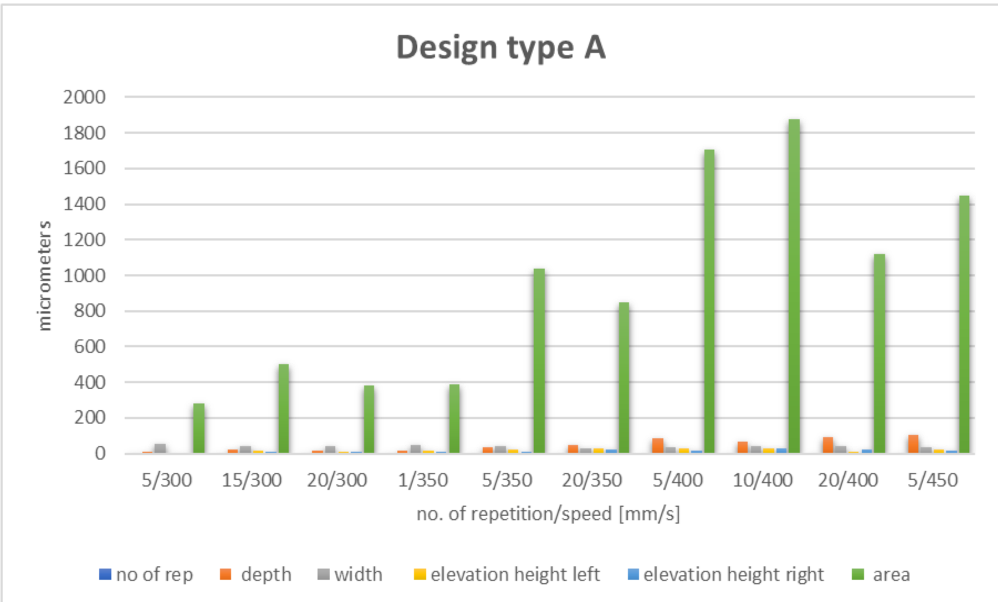

Figure 4.23. Geometry characterization of hollow and recast material after LST for octagonal donuts pattern (design type A).

4.1.2. Design type B, ellipses at 90° pattern

In the case of type B design the grooves are wider and shallower than for the other two designs. This is a consequence of the expelled material that has been deposited inside the groove at a lower position than in design type A. The results indicate an increase in width with the scanning speed increasing, while the recast material elevation and area of depth displaying a relatively constant tendency.

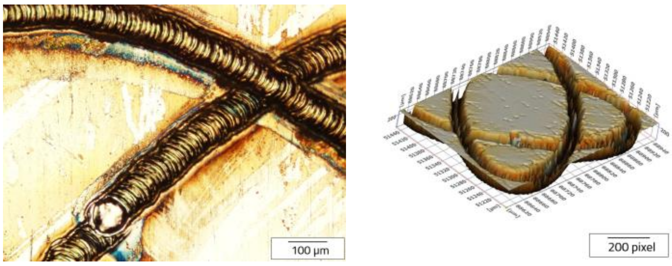

(a) (b)

Figure 4.24. Microscopic image (a) and 3D topographic image (b) of LST design type B, frequency 30 kHz, speed 300 mm/s, no. of repetition 1.

In the Figure 4.25 is presented microscopic images and 3D optical map micrograph of the sample B (speed 300 mm/s, frequency 30 kHz, no. of repetition 10, pulse duration 170 ns).

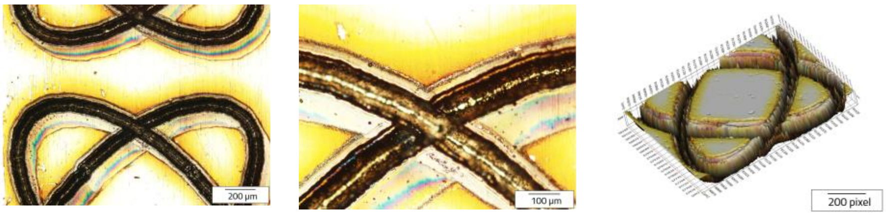

(a) (b) (c)

Figure 4.25. Microscopic image (a, b) and 3D topographic image (c) of LST design type B, frequency 30 kHz, speed 300 mm/s, no. of repetition 10.

In the Figure 4.26. is presented microscopic images and 3D optical map micrograph of the sample B (speed 300 mm/s, frequency 30 kHz, no. of repetition 15, pulse duration 170 ns). The measurements with the optical microscope on the cross-section images achieved offers an average area of 1556.35 μm^2, with 54.94 µm depth and 28.31 µm width. The recast material on the left side has 8.03 µm height and the right side has 20.62 µm height. Splashes appear asymmetrically due to inclination of the laser beam.

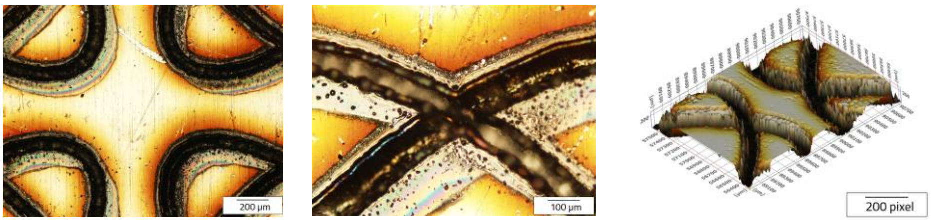

(a) (b) (c)

Figure 4.26. Microscopic image (a, b) and 3D topographic image (c) of LST design type B, frequency 30 kHz, speed 300 mm/s, no. of repetition 15.

In the Figure 4.27. is presented microscopic image and 3D optical map micrograph of the sample B (speed 300 mm/s, frequency 30 kHz, no. of repetition 20, pulse duration 170 ns). The measurements with the optical microscope on the cross-section images achieved offers an average area of 2539.36 μm^2, with 43.82 µm depth and 57.95 µm width. The recast material on the left side has 18.07 µm height and the right side has 22.24 µm height.

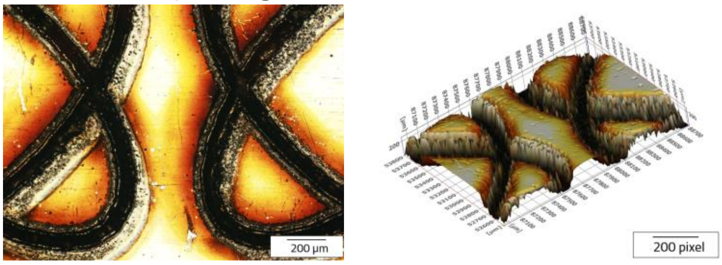

(a) (b)

Figure 4.27. Microscopic image (a) and 3D topographic image (b) of LST design type B, frequency 30 kHz, speed 300 mm/s, no. of repetition 20.

In the Figure 4.28.c. is highlighted the phenomenon of the imperfect trajectory of the geometrical pattern and the beginning and the end of LST process being decentered, the loop closure defect.

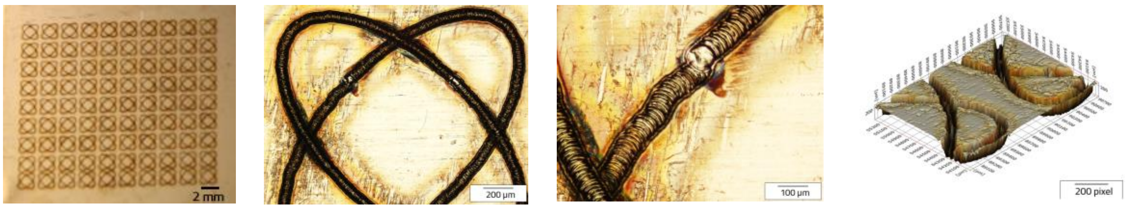

(a) (b) (c) (d)

Figure 4.28. Image detail (a), microscopic images (b, c) and 3D topographic image (d) of LST design type B, frequency 35 kHz, speed 350 mm/s, no. of repetition 1.

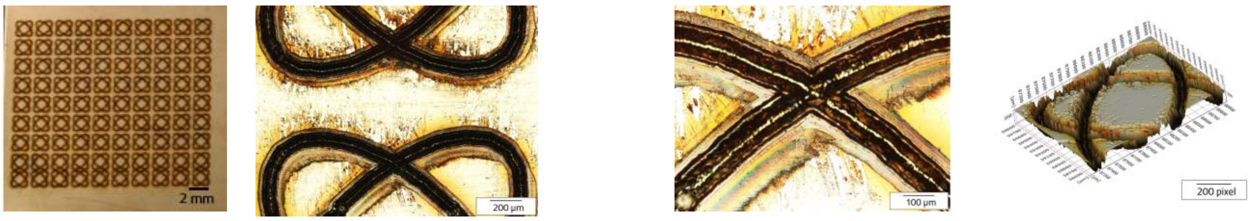

(a) (b) (c) (d)

Figure 4.29. Image detail (a), microscopic images (b, c) and 3D topographic image (d) of LST design type B, frequency 35 kHz, speed 350 mm/s, no. of repetition 5.

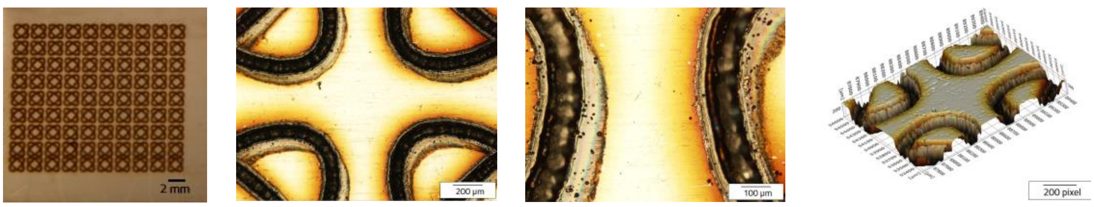

(a) (b) (c) (d)

Figure 4.30. Image detail (a), microscopic images (b, c) and 3D topographic image (d) of LST design type B, frequency 35 kHz, speed 350 mm/s, no. of repetition 10.

From the Figure 4.31 can be visible the overlap surface of the two ellipses, creating a higher influenced HAZ. No splashes can be seen for this pattern.

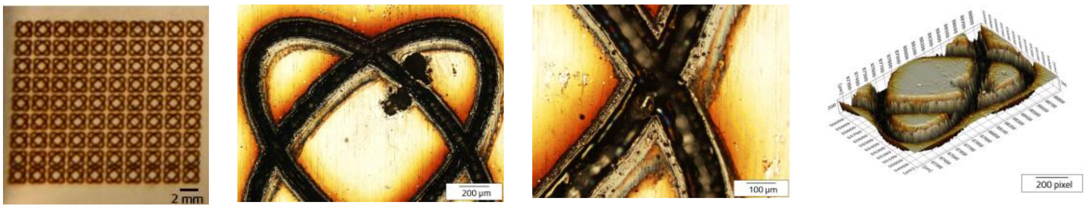

(a) (b) (c) (d)

Figure 4.31. Image detail (a), microscopic images (b, c) and 3D topographic image (d) of LST design type B, frequency 35 kHz, speed 350 mm/s, no. of repetition 15.

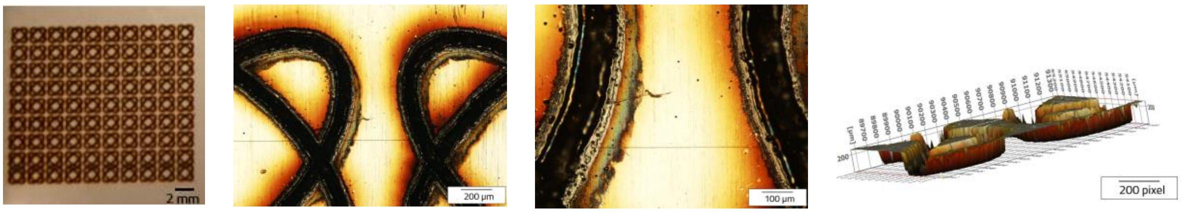

(a) (b) (c) (d)

Figure 4.32. Image detail (a), microscopic images (b, c) and 3D topographic image (d) of LST design type B, frequency 35 kHz, speed 350 mm/s, no. of repetition 20.

It becomes clearer and more evident whit the increase of speed and frequency that this pattern offers an imperfect trajectory (Figure 4.33.b.).

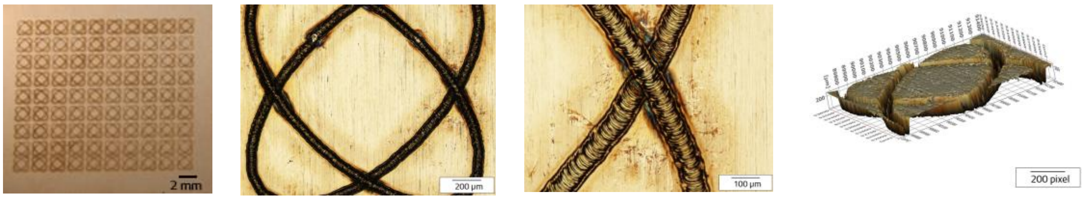

(a) (b) (c) (d)

Figure 4.33. Image detail (a), microscopic images (b, c) and 3D topographic image (d) of LST design type B, frequency 40 kHz, speed 400 mm/s, no. of repetition 1.

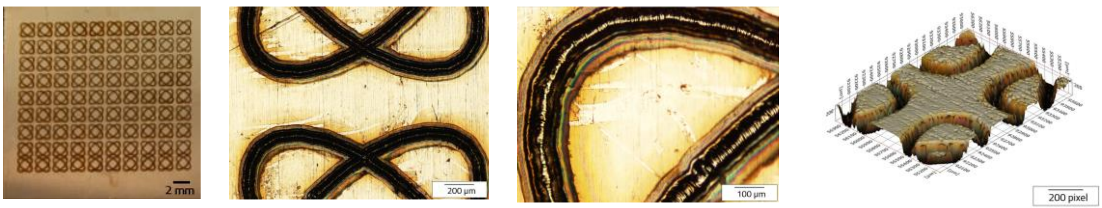

(a) (b) (c) (d)

Figure 4.34. Image detail (a), microscopic images (b, c) and 3D topographic image (d) of LST design type B, frequency 40 kHz, speed 400 mm/s, no. of repetition 5.

In the Figure 4.37 is presented image detail of micro texturing pattern, microscopic images and 3D optical map micrograph of the sample B (speed 400 mm/s, frequency 40 kHz, no. of repetition 20, pulse duration 120 ns). The measurements with the optical microscope on the cross-section images achieved offers 39.86 μm depth and 63.97 μm width. The recast material on the left side has 17.61 μm height and the right side has 20.66 μm height.

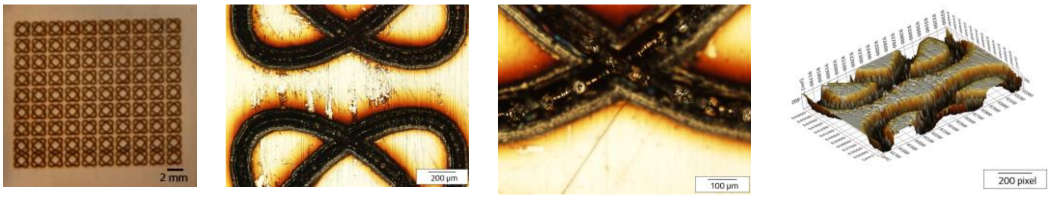

(a) (b) (c) (d)

Figure 4.37. Image detail (a), microscopic images (b, c) and 3D topographic image (d) of LST design type B, frequency 40 kHz, speed 400 mm/s, no. of repetition 20.

In the Figure 4.45 is presented image detail of micro texturing pattern and microscopic images of the sample B (speed 500 mm/s, frequency 50 kHz, no. of repetition 10, pulse duration 90 ns). The measurements with the optical microscope on the cross-section images achieved offers 38.01 μm depth and 64.42 μm width. The recast material on the left side has 16.75 μm height and the right side has 20.62 μm height.

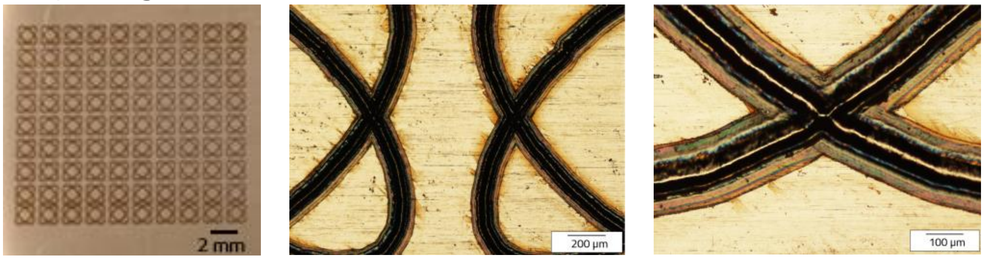

(a) (b) (c)

Figure 4.45. Image detail (a) and microscopic images (b, c) of LST design type B, frequency 50 kHz, speed 500 mm/s, no. of repetition 10.

With increased speed and frequency, for a single pass, it becomes difficult to highlight the micro-textured pattern (Figure 4.54.) and as the number of repetitions increases, the width of the micro texture decreases (Figure 4.55.).

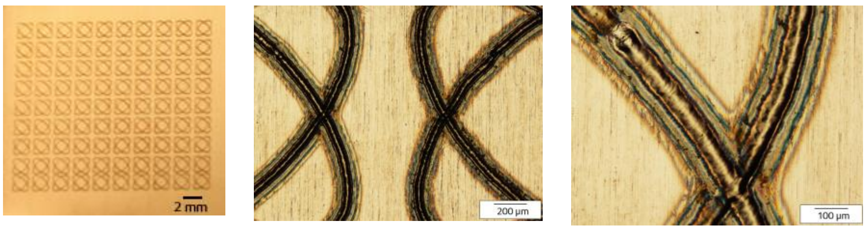

(a) (b) (c)

Figure 4.54. Image detail (a) and microscopic images (b, c) of LST design type B, frequency 65 kHz, speed 650 mm/s, no. of repetition 5.

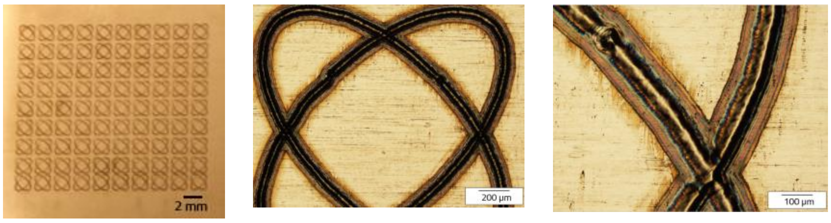

(a) (b) (c)

Figure 4.55. Image detail (a) and microscopic images (b, c) of LST design type B, frequency 65 kHz, speed 650 mm/s, no. of repetition 10.

In Figure 4.68 the results indicate an increase in width with the scanning speed increasing, while the recast material elevation and area of depth displaying a relatively constant tendency. The parameter width for upward trend stops at 400 mm/s speed, 40 kHz frequency and 20 no. of repetitions. After this parameter, the tendency is to decrease. Not same trend can by say about elevation area on the left and right side (recast material), and area. The area is influenced by the depth of the hollow in a fluctuation trend (low/high).

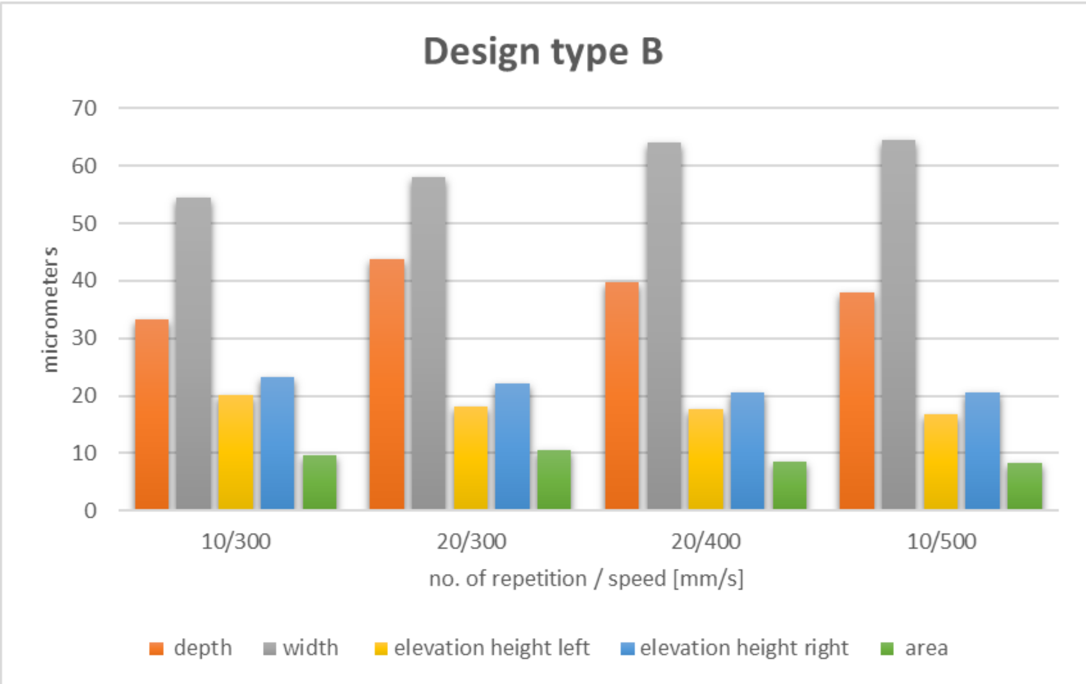

Figure 4.68. Geometry characterization of hollow and recast material after LST for ellipses at 90° pattern (design type B).

4.1.3. Design type C, dimple/hole/crater array pattern

In the case of design type the lack of elevation of the recast material can be noticed. Due to this fact, the elevation's height is missing. With the increase in speed, depth, width, an area decreasing has been remarked. The large number of splashes near the outline of the crater can be noticed (Figure 4.69).

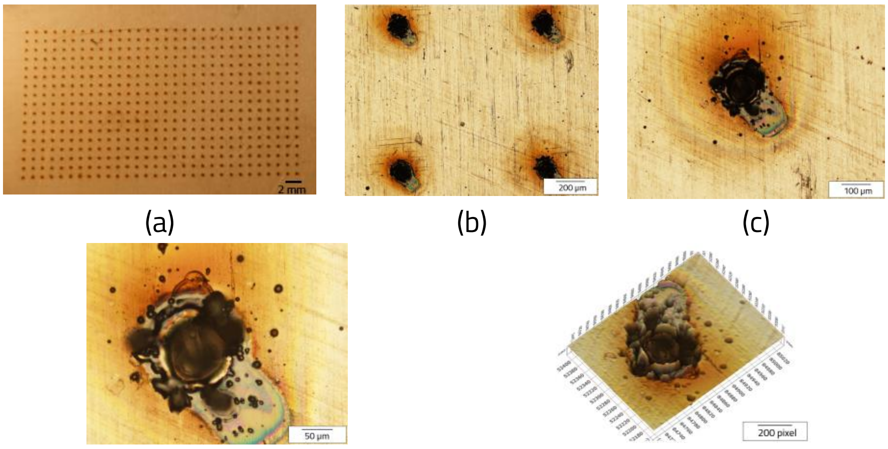

(a) (b) (c)

(d) (e)

Figure 4.69. Image detail (a) and microscopic images (b, c, d) and 3D topographic image (e) of LST design type C, frequency 30 kHz, speed 300 mm/s, no. of repetition 1.

In the Figure 4.70. are presented the image detail of the micro texture applied and microscopic images of the sample C (speed 300 mm/s, frequency 30 kHz, no. of repetition 5, pulse duration 170 ns). The measurements with the optical microscope on the cross-section images achieved offers an average area of 18,237.98 µm^2, with 126.82 µm depth and 143.81 µm width. There is no recast material on the edges of the crevasse.

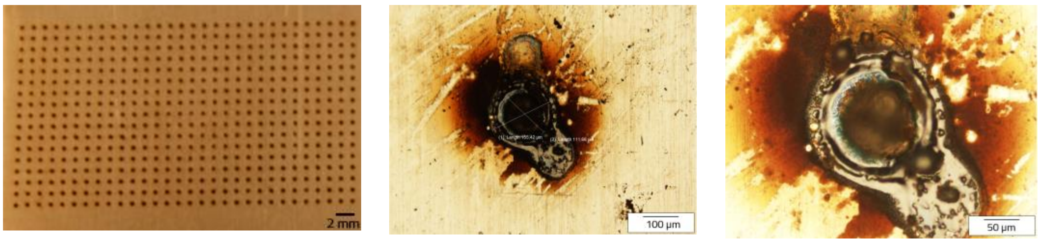

(a) (b) (c)

Figure 4.70. Image detail (a) and microscopic images (b, c) of LST design type C, frequency 30 kHz, speed 300 mm/s, no. of repetition 5.

In the Figure 4.71 are presented the image detail of the micro texture applied, microscopic images and cross-section optical micrograph of the sample C (speed 300 mm/s, frequency 30 kHz, no. of repetition 10, pulse duration 170 ns). The measurements with the optical microscope on the cross-section images achieved offers an average area of 3807.80 µm^2, with 127.64 µm depth and 156.65 µm width. There is no recast material on the edges of the crevasse. From the cross-section microscope image can be observed the lack of the recast material (Figure 4.71.e).

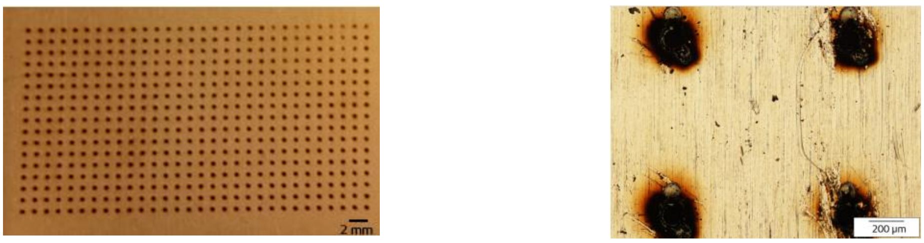

(a) (b)

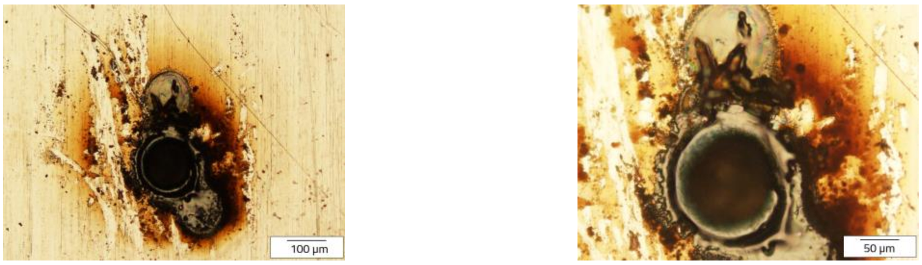

(c) (d)

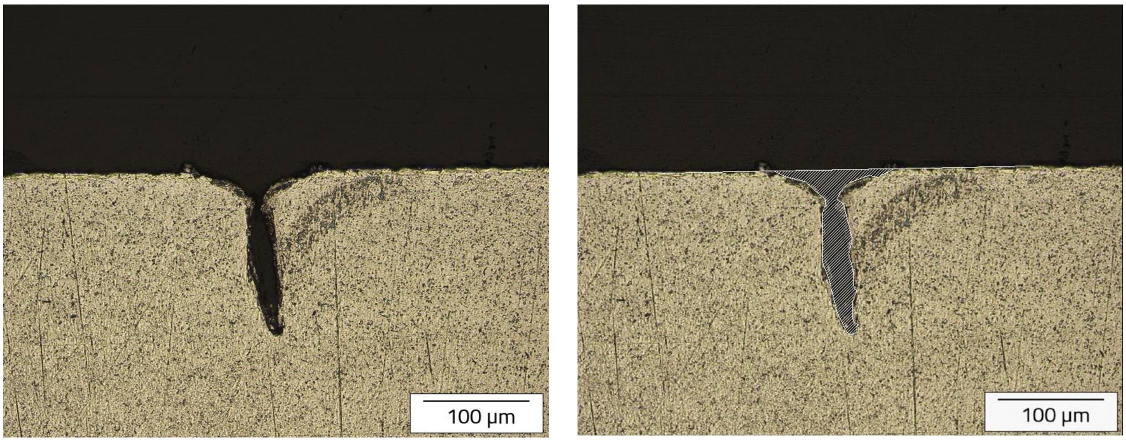

(e) (f)

Figure 4.71. Image detail (a), microscopic images (b, c, d) and cross-section (e) of LST design type C, (f) measurements, frequency 30 kHz, speed 300 mm/s, no. of repetition 10.

In the Figure 4.72 are presented the image detail of the micro texture applied, microscopic images and cross-section optical micrograph of the sample C (speed 300 mm/s, frequency 30 kHz, no. of repetition 15, pulse duration 170 ns). The measurements with the optical microscope on the cross-section images achieved offers an average area of 3428.54 μm^2, with 157.34 μm depth and 124.95 μm width. There is no recast material on the edges of the crevasse (Figure 4.72.e).

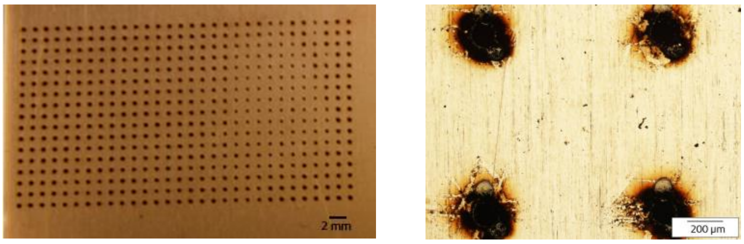

(a) (b)

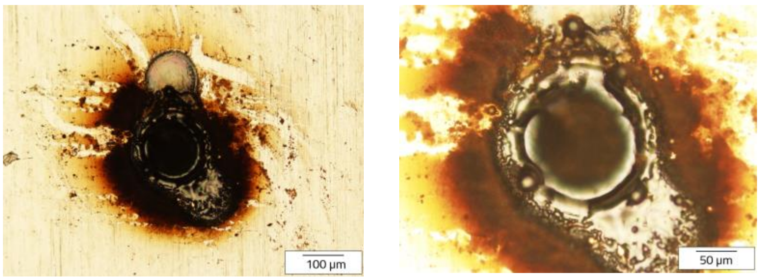

(c) (d)

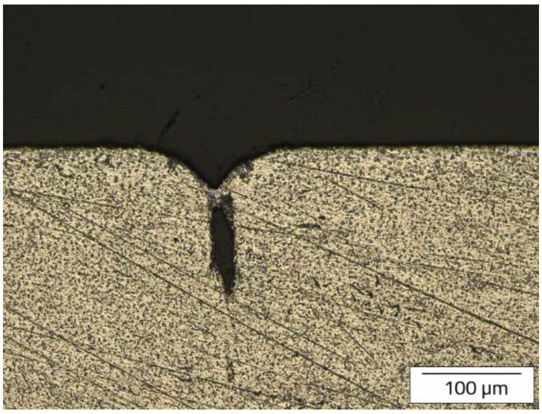

(e)

Figure 4.72. Image detail (a), microscopic images (b, c, d) of LST design type C, frequency 30 kHz, speed 300 mm/s, no. of repetition 15.

With increased speed, frequency, and number of repetitions the HAZ becomes larger and more pronounced. The splashes are no longer so obvious as at a lower frequency and a lower number of repetitions, which may mean that they are no longer close to the edges of the hollow, in the thermally affected area. There is a possibility that the splashes from a micro textured point to be displaced to another point, or worse to be displaced in neighbour hollow, creating erroneous values of crevice depth.

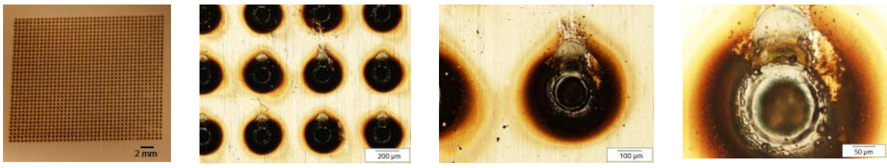

(a) (b) (c) (d)

Figure 4.84. Image detail (a), microscopic images (b, c, d) of LST design type C, frequency 45 kHz, speed 450 mm/s, no. of repetition 15.

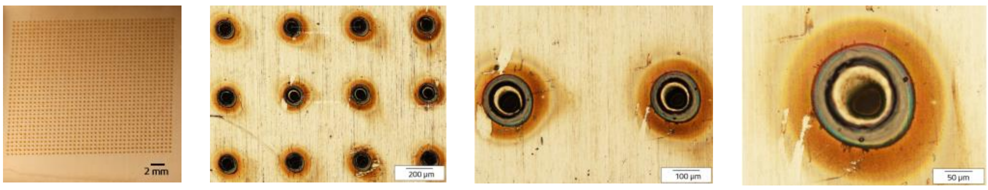

(a) (b) (c) (d)

Figure 4.85. Image detail (a), microscopic images (b, c, d) of LST design type C, frequency 50 kHz, speed 500 mm/s, no. of repetition 1.

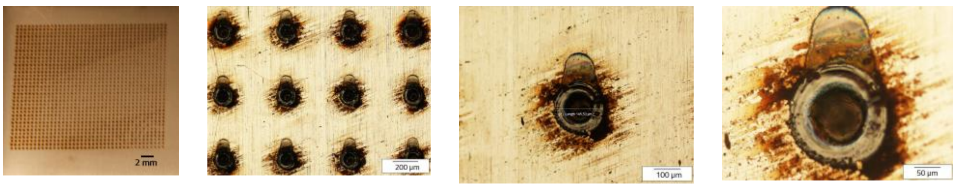

(a) (b) (c) (d)

Figure 4.86. Image detail (a), microscopic images (b, c, d) of LST design type C, frequency 50 kHz, speed 500 mm/s, no. of repetition 5.

With increased speed, frequency, and number of repetitions the HAZ becomes larger and more pronounced. The splashes are no longer so obvious as at a lower frequency and a lower number of repetitions, which may mean that they are no longer close to the edges of the hollow, in the thermally affected area. There is a possibility that the splashes from a micro textured point to be displaced to another point, or worse to be displaced in neighbour hollow, creating erroneous values of crevice depth.

In the Figure 4.87 are presented the image detail of the micro texture applied and microscopic images of the sample C (speed 500 mm/s, frequency 50 kHz, no. of repetition 15, pulse duration 90 ns). The measurements with the optical microscope on the cross-section images achieved offers an average area of 2608.70 μm^2, with 48.39 μm depth and 110.75 μm width. There is no recast material on the edges of the crevasse.

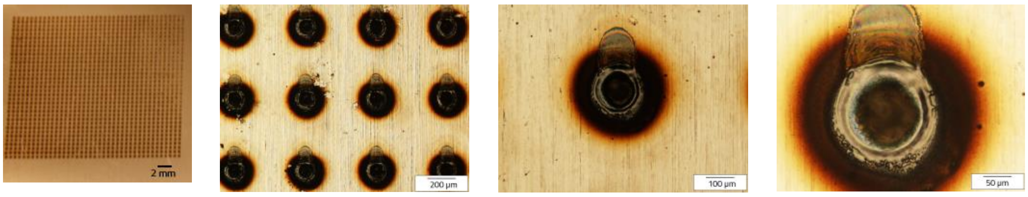

(a) (b) (c) (d)

Figure 4.87. Image detail (a), microscopic images (b, c, d) of LST design type C, frequency 50 kHz, speed 500 mm/s, no. of repetition 10.

In the Figure 4.89 are presented the image detail of the micro texture applied, microscopic images and cross-section optical micrograph of the sample C (speed 600 mm/s, frequency 60 kHz, no. of repetition 1, pulse duration 80 ns). The measurements with the optical microscope on the cross-section images achieved offers an average area of 2608.70 μm^2, with 48.39 μm depth and 110.75 μm width. There is no recast material on the edges of the crevasse.

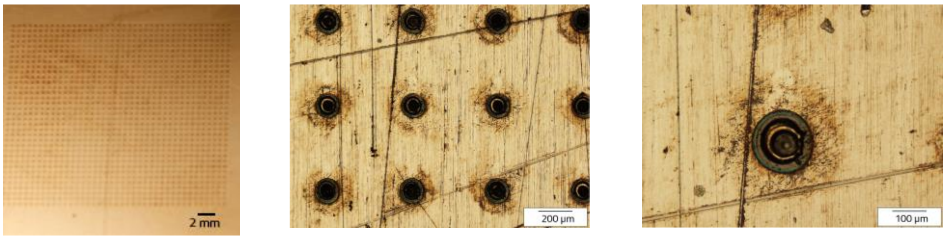

(a) (b) (c)

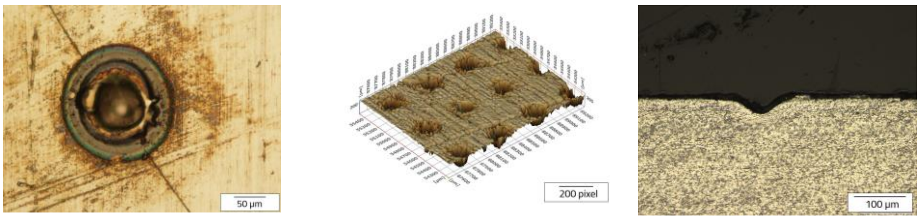

(d) (e) (f)

Figure 4.89. Image detail (a) and microscopic images (b, c, d), 3D topographic image (e) and cross-section view (f) of LST design type C, frequency 60 kHz, speed 600 mm/s, no. of repetition 1.

In the case of design type C the lack of elevation of the recast material can be noticed. Due to this fact, the elevation's height is missing from Figure 4.104. With the increase in speed, depth, width and area decreasing has been remarked. The best outcome is for a minimum 10 number of repetitions, but with increasing frequency and speed, a decreasing trend is created among the results of measurements of micro textures.

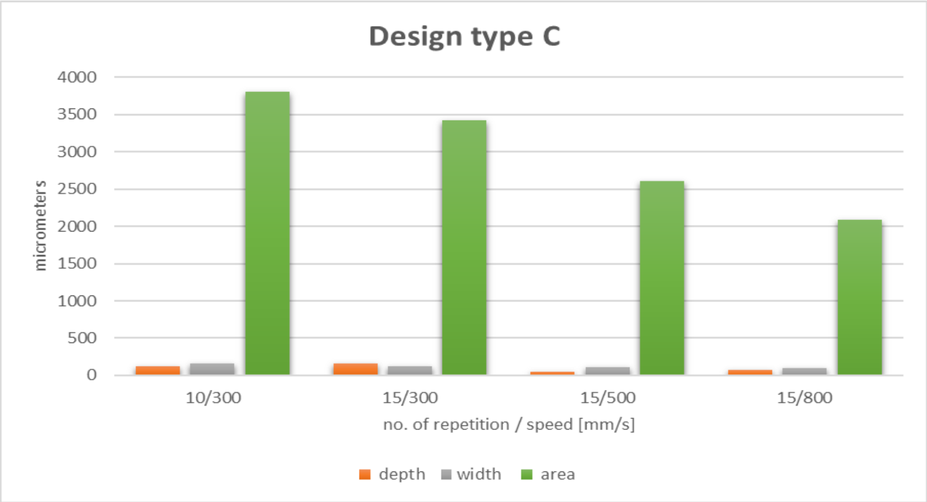

Figure 4.104. Geometry characterization of hollow after LST for dimple/hole/crater array pattern (design type C).

4.2. Scanning electronic microscopy

4.2.1. Octagonal donuts micro texturing pattern design A

From the top view images (Figure 4.105), acquired with scanning electron microscopy, it can be observed a difference in size of the heat affected zone and recast material (right side is larger), caused by angle of laser beam (3° to the left). In the right view of Figure 4.105 it can be noticed the continuous groove (successive contours), similar to the seam weld due to the 99% overlapping of the laser spot.

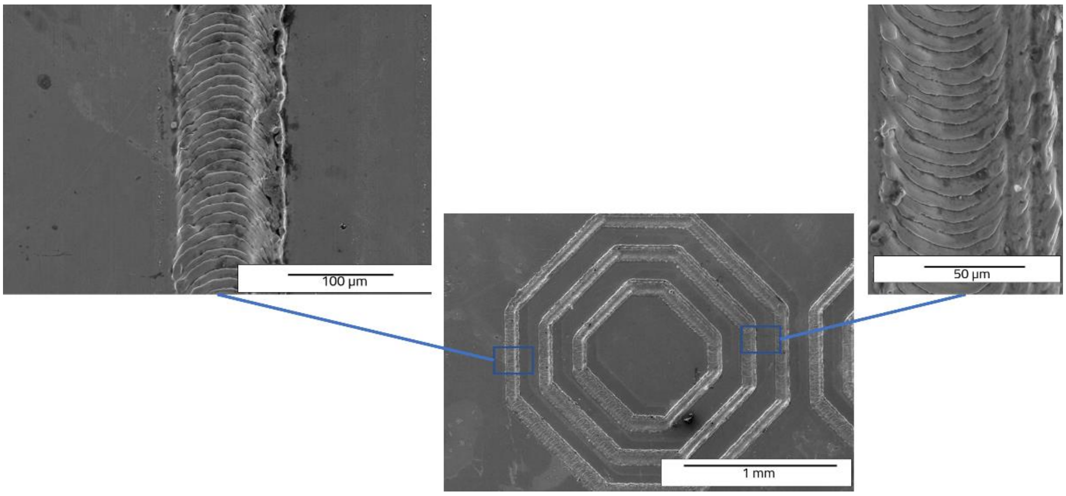

Figure 4.105. Top view SEM images of octagonal donuts shape (design type A) of LST, frequency 30 kHz, speed 300 mm/s and no. of repetition 10.

Another observation can be made regarding the splashes (Figures 4.105-4.107). When the frequency and speed are increased, the expulsed material is exceeding the edges of the groove in the form of splashes and not in the form of recast material.

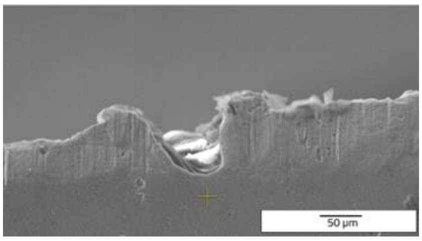

(a)

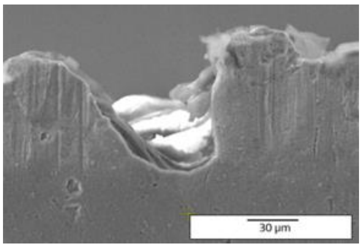

(b)

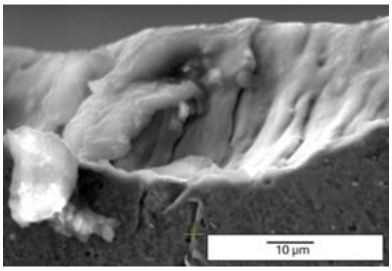

(c)

Figure 4.106. Cross-section SEM images of octagonal donuts shape (design type A) of LST, frequency 30 kHz, speed 300 mm/s and no. of repetition 10.

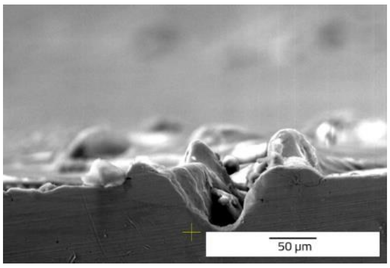

(a)

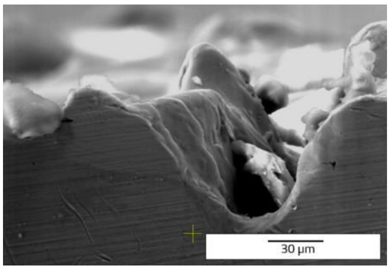

(b)

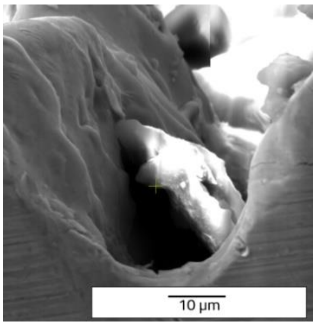

(c)

Figure 4.107. Cross-section SEM images of octagonal donuts shape (design type A) of LST, frequency 40 kHz, speed 400 mm/s and no. of repetition 10.

4.2.2. Ellipses at 90° micro texturing pattern design B

In the ellipse pattern case, can be observed more splashes and a lower deposition as recast material (Figure 4.108). The recast material is higher on a side than the other, same ground as presented for previous pattern (angle of the laser beam axis).

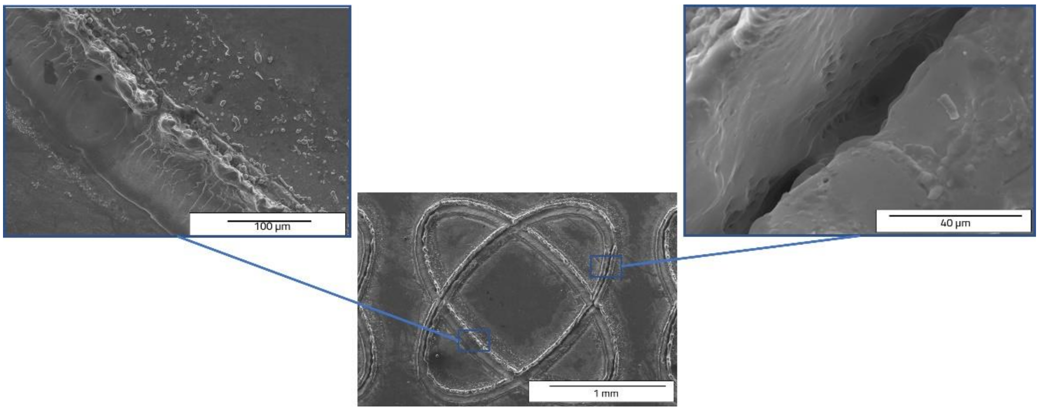

Figure 4.108. Top view SEM images of ellipses at 90° shape (design type B) of LST, frequency 30 kHz, speed 300 mm/s and no. of repetition 10.

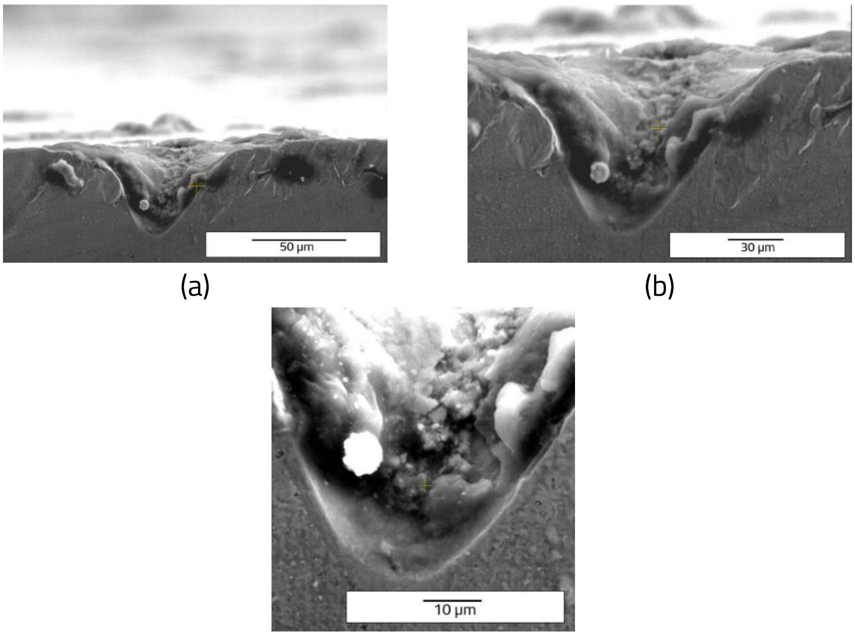

(a) (b)

(c)

Figure 4.109. Cross-section SEM images of ellipses at 90° shape (design type B) of LST, frequency 30 kHz, speed 300 mm/s and no. of repetition 10.

4.2.3. Dimple/hole/crater array micro texturing pattern design C

For crater array pattern is outlined a very low recast material and, in many cases, completely missing (Figures 4.110-4.111).

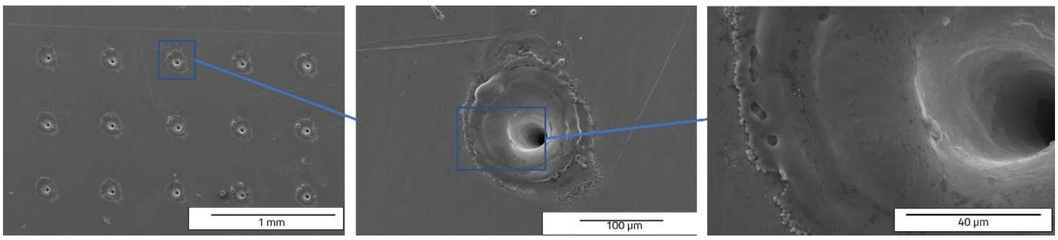

Figure 4.110. Top view SEM images of crater array shape (design type C) of LST, frequency 30 kHz, speed 300 mm/s and no. of repetition 10.

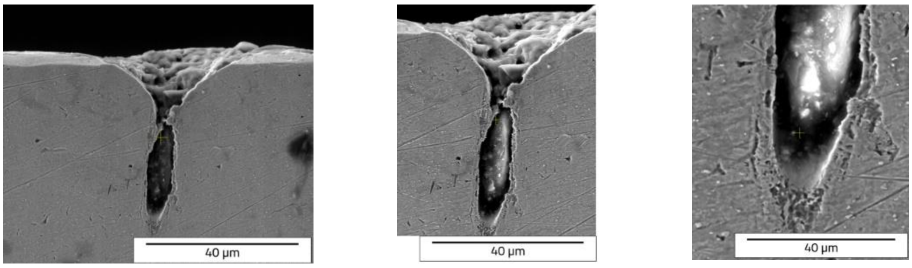

(a) (b) (c)

Figure 4.111. Cross-section SEM images of crater array (design type C) of LST, frequency 30 kHz, speed 300 mm/s and no. of repetition 10.

One can notice the keyhole shape of the crater array shape (design type C) (Figures 4.111 and 4.116), different from that of V grooves of the designs type A and type B. This keyhole shape is specific to laser welding, as described in [27,111].

4.3. EDX analysis

4.3.1. Octagonal donuts micro texturing pattern design A

The EDX (Energy Dispersive X-Ray) elemental analysis display a low variation (from recast material to the deepest point of the hollow and to heat affected zone) of the elements regarding the weight and atomic percentage. The elemental analysis shows a zero-weight percentage for oxygen, which does not apply for the ellipse and crater array patterns.

Table 4.1. EDX elemental analysis of micro textured design octagonal donuts shape (design type A).

Element / Point	Iron		Chromium		Carbon	
	weight %	atomic %	weight %	atomic %	weight %	atomic %
1	70.58	42.78	11.85	7.72	17.57	49.5
2	72.24	47.16	13.47	9.44	14.29	43.39
3	65.55	35.72	11.82	6.92	22.64	57.36
4	70.54	44.69	13.90	9.46	15.56	45.85

Elemental analysis of octagonal micro structuring, cross-sectional images (Figure 4.112) show a uniform spread outside the hollow area, excepting carbon also present in the cavity wall area. Figure 4.113 shows the main elements on the EDX spectrum (Cr, Fe, C).

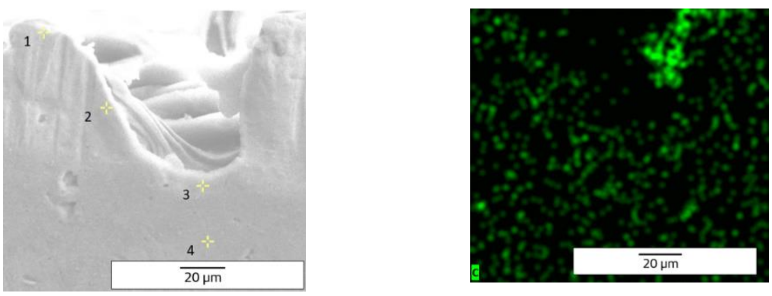

(a) (b)

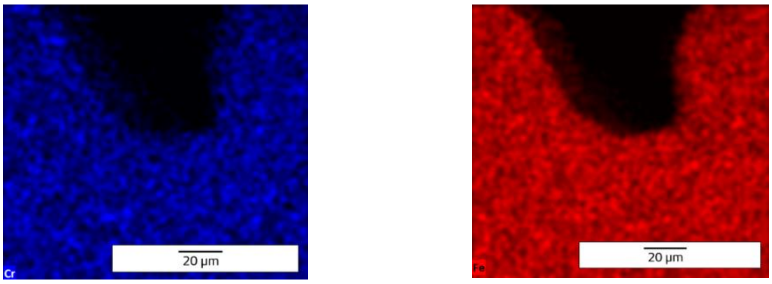

(c) (d)

Figure 4.112. EDX elemental analysis of micro textured design octagonal donuts shape (design type A) image of measurement points (a) and elemental mapping images (b-C, c-Cr, d-Fe).

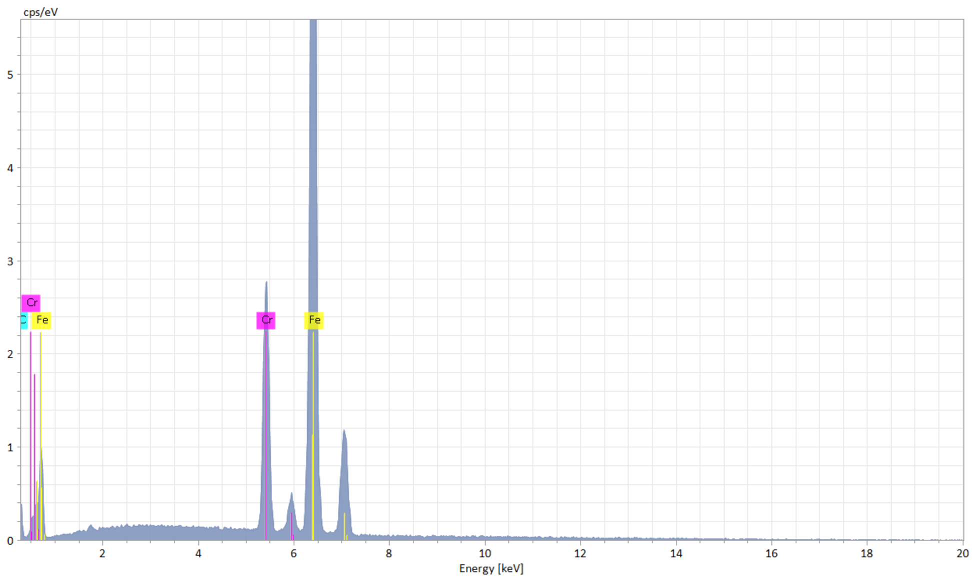

Figure 4.113. EDX spectrum of micro textured design octagonal donuts shape (design type A).

4.3.2. Ellipses at 90° micro texturing pattern design B

For ellipse pattern, a difference is the appearance of oxygen for the measurement point 2 and 3, meaning the absence of the oxygen element in the recast material and heat affected zone (Table 4.2). When oxygen is part of the measurement point is observed a decreasing of iron and chromium and carbon increasing.

Table 4.2. EDX elemental analysis of micro textured design ellipses at 90° shape (design type B).

Element / Point	Iron		Chromium		Carbon		Oxygen	
	weight %	atomic %	weight %	atomic %	weight %	atomic %	weight %	atomic %
1	75.22	54.18	14.43	11.16	10.35	34.66	-	-
2	57.79	28.61	12.12	6.45	22.56	51.93	7.53	13.01
3	58.98	29.16	10.70	5.68	22.41	51.51	7.91	13.65
4	76.52	57.35	14.62	11.76	8.86	30.88	-	-

The carbon is spread just where is the cavity (see the cross-section images of EDX analysis from Figure 4.114) and the other elements (Cr, Fr and O) spreading is wide.

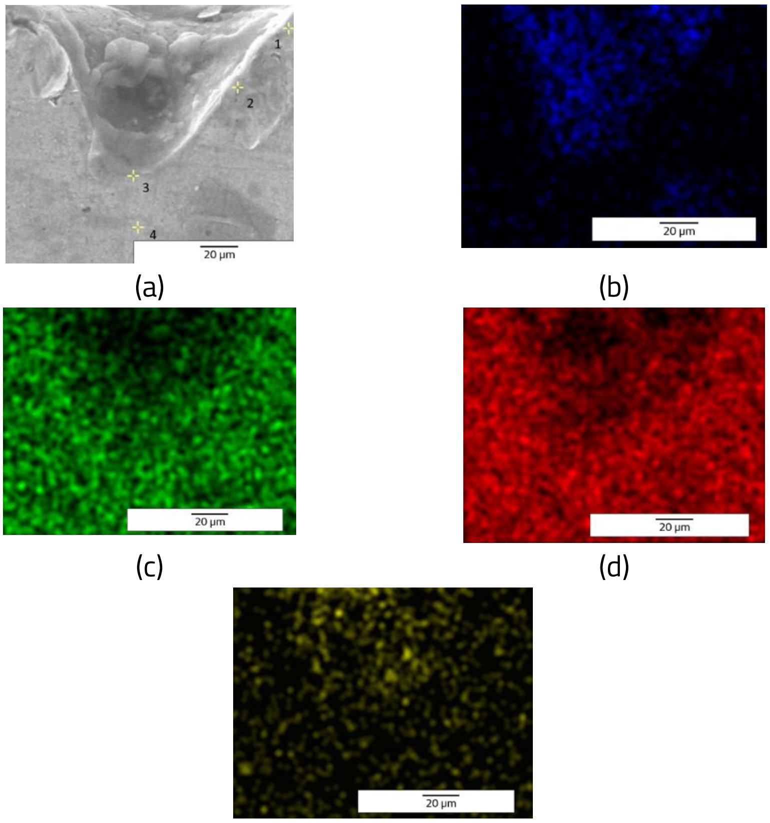

(a) (b)

(c) (d)

(e)

Figure 4.114. EDX elemental analysis of micro textured design ellipses at 90° shape (design type B) image of measurement points (a) and elemental mapping images (b-C, c-Cr, d-Fe, e-O).

Figure 4.115 shows the main elements on the EDX spectrum (Cr, O, Fe, C).

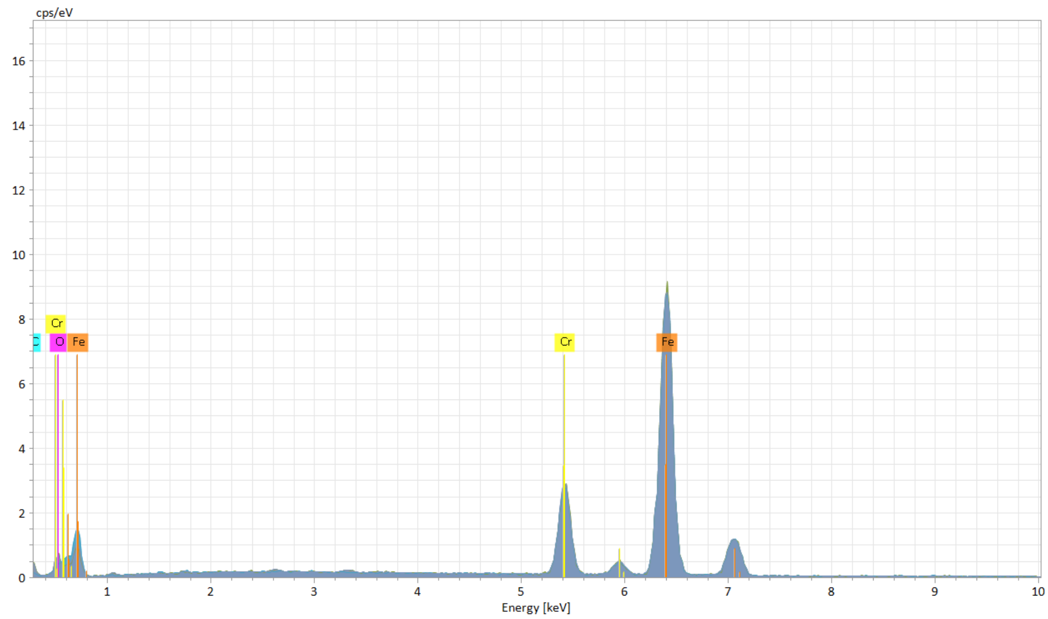

Figure 4.115. EDX spectrum of micro textured design ellipses at 90° shape (design type B).

4.3.3. Dimple/hole/crater array micro texturing pattern design C

The crater array model required more EDX measurement points due to the larger gaps created by the LST (Table 4.3). The same result, as the ellipse model, is for the carbon element (only in the cavity area). The highest percentage by weight of carbon is at the bottom of the crater (Figure 4.116), and the lowest percentage by weight is in the area affected by heat. Oxygen is less widespread than in previous models (donuts and octagonal ellipses).

Table 4.3. EDX elemental analysis of micro textured design crater array shape (design type C).

Element / Point	Iron		Chromium		Carbon		Oxygen	
	weight %	atomic %	weight %	atomic %	weight %	atomic %	weight %	atomic %
1	76.42	56.67	14.33	11.41	9.26	31.92	-	-
2	78.41	62.50	14.92	12.77	6.67	24.73	-	-
3	72.10	47.98	13.61	9.73	11.79	36.47	2.50	5.82
4	59.96	30.50	11.32	6.19	20.91	49.45	7.81	13.87
5	77.56	60.92	15.27	12.88	7.17	26.20	-	-

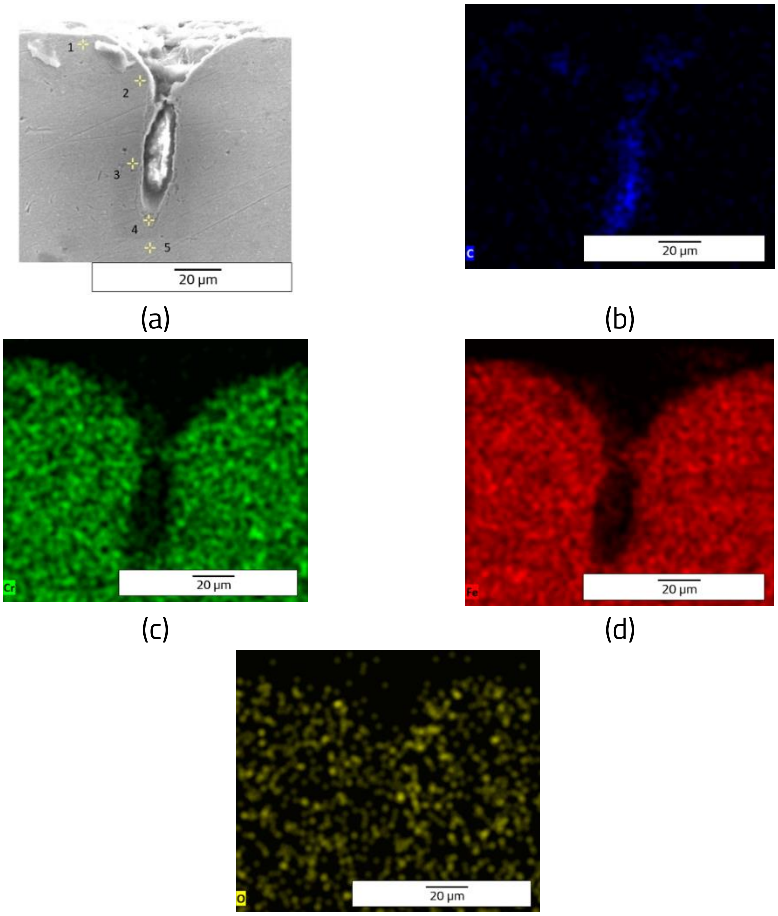

(a) (b) (c) (d) (e)

Figure 4.116. EDX elemental analysis of micro textured design crater array shape (design type C) image of measurement points (a) and elemental mapping images (b-C, c-Cr, d-Fe, e-O).

Figure 4.117. shows the main elements on the EDX spectrum (Cr, O, Fe, C).

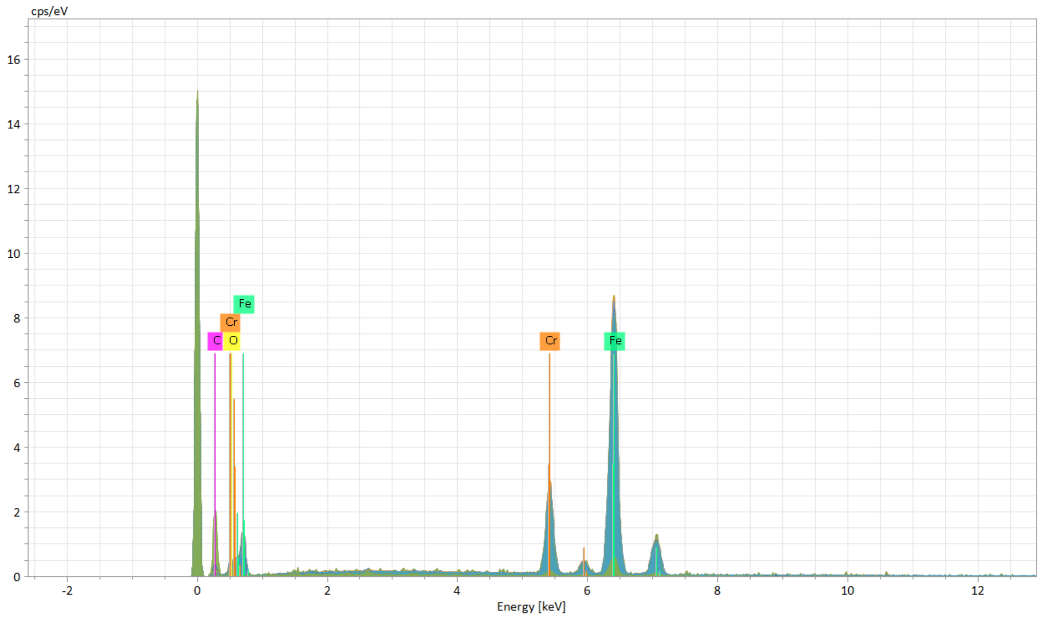

Figure 4.117. EDX spectrum of micro textured design crater array shape (design type C).

4.4. Conclusions

Even if the same frequency, speed, and number of repetitions were used for designs A, B and C, the geometry of applied microstructure has an important role. From the cross-section optical micrographs and profile histograms, it can be observed that material displacement is less evident for pattern type B, comparing with patterns type A and C. The same remark can be made in the case of pattern type C in comparison with patterns type B and A (after 10 repetitions of LST operation) regarding the pull-out material.

The SEM images (top view and cross-section) offers information about the phenomena that occur during LST. The crater array (design type C) and octagonal (design type A) patterns present o low area of splashes compared to ellipse pattern (design type B). The same phenomenon occurs in the case of recast material, which occurs in the case of octagonal and ellipse patterns, due to the 99% overlapping of the laser spot. In the case of the crater array, where there is no overlapping, the recast material is almost non-existent.

In two out of three patterns is pointed the presence of the oxygen element, which is beneficial for ferritic stainless steel in creating the passive layer (an oxide layer, formed from chromium and oxygen and has an inert reaction to the environment).

In the area of the recast material, the EDX analysis is pointing out almost a double value for the carbon element (weight %) for octagonal pattern. The results, for ellipse and crater array patterns, are very appropriate (iron, chromium and the carbon elements). At the bottom of the groove, the pattern that offers different results for elemental analysis is the octagonal design. In the thermally affected area, the measured values of the elemental analysis are appropriate for all the patterns. The cross-section images of EDX analysis offers the answer that nothing is changed, regarding micro textured area.

Morphological analysis provides valuable information about the microrelief of laser textured surfaces, clues for mechanical interlocking in the case of hybrid joints. Of the three analyzed models, the highest level of recast material is observed for design type A, being more recommended its application for the preparation of the metal surface before hybrid welding.

The best outcome for joining dissimilar materials is the pattern design type A, speed 300 mm/s, frequency 30 kHz, no. of repetition 15, pulse duration 170 ns. The parameters resulted from the measurements are: depth of 19.53 μm, 499.06 $μm^2$ for the area, top width at the plate surface 40.29 μm, middle width 30.11 μm and low width 12.10 μm. The recast material on the left side has an area of 75.57 $μm^2$ with 5.526 μm height. The right recast side has an area of 187.73 $μm^2$ and 9.12 μm height. The hollow is almost symmetrical, with a good depth and without the expulsed material collapsed into, offering a good option for mechanical interlocking. The expulsed material as recast material can behave as drag in joining dissimilar materials.

For tribological applications, the best outcome is for pattern design type C. The measurements, from cross-section microscopic images, are: 157.37 μm for depth, 124.95 μm for the width at surface, 22.83 μm for low width and 3428.54 $μm^2$ for the area of the hollow. The parameter with a considerable outcome is for 30 kHz frequency, 300 mm/s speed and no. of repetitions 15 micro texturing, offering vast possibilities for tribological applications uses, due to the lack of recast material. In the case of pattern B, more research is recommended.

5. Roughness analysis of Laser Surface Texturing of AISI 430 Stainless Steel

All parameters measured are from roughness profile (R-profile, according to EN ISO 4287 and EN ISO 16610-21).

5.1. Results and discussion

The roughness of the sample without laser surface texturing (LST) was obtained in the conditions presented in the chapter 3.7, kept constant during experiments:

- R_a = 0.681 μm,
- R_z = 2.253 μm,
- R_t = 8.828 μm.

5.1.1. Design type A, octagonal donuts pattern

Overall, the results show an increasing in the surface roughness compared to the surface roughness of the sample without LST (Figure 5.1).

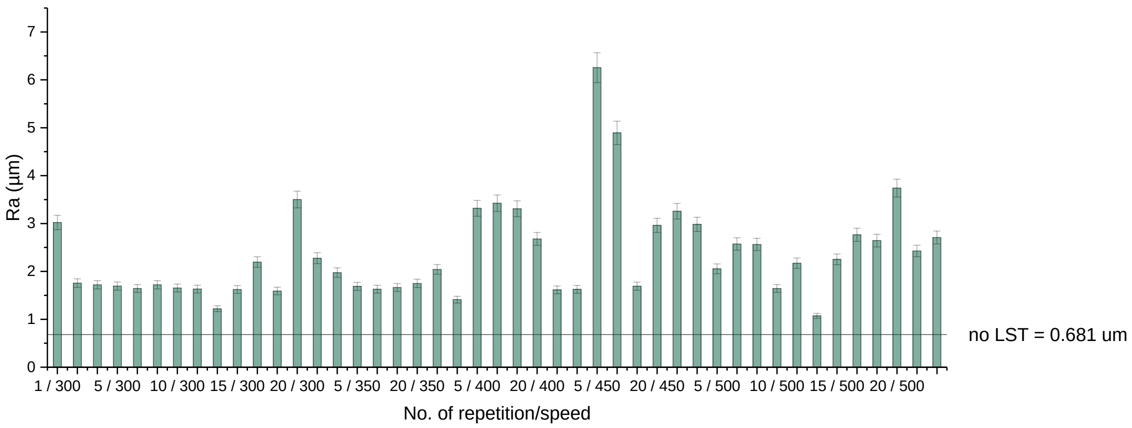

(a)

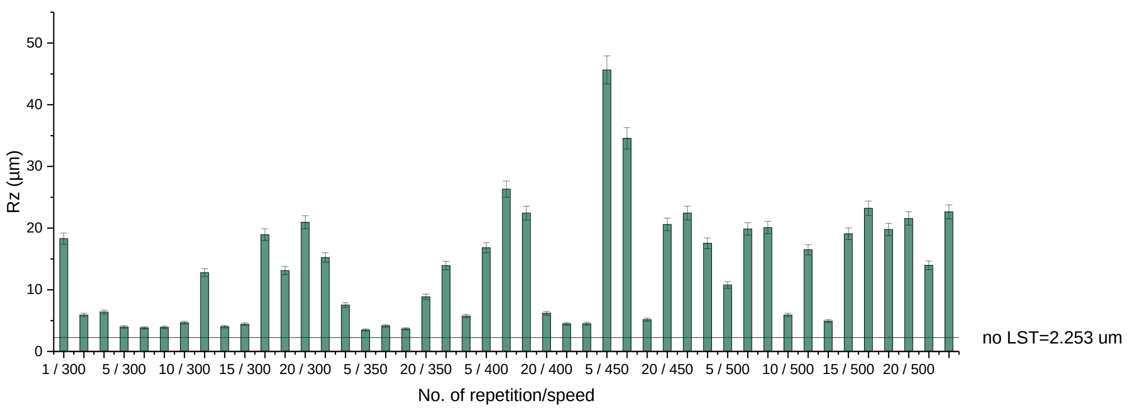

(b)

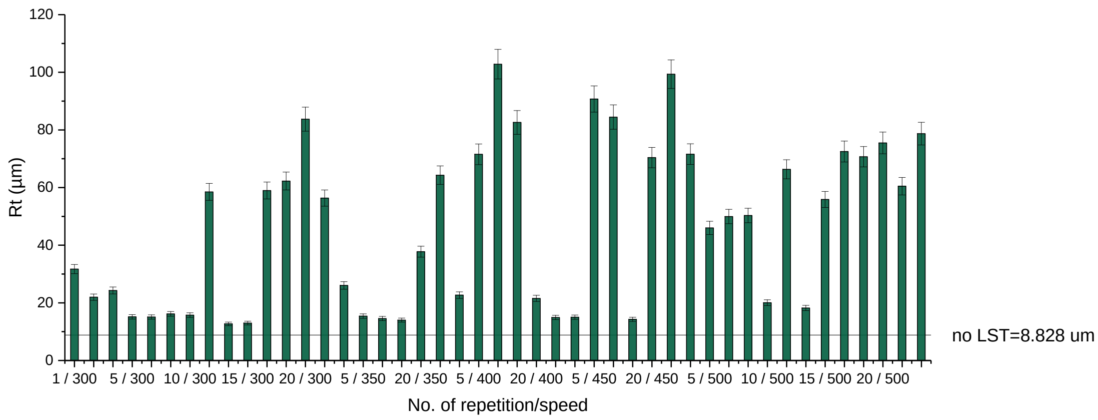

(c)

Figure 5.1. Surface roughness charts for design type A, R_a — arithmetical mean deviation of profile (a), R_z — total peak-to-valley- height (b) and R_t — ten-point height of irregularities (c).

Figure 5.2 presents the variation of roughness parameters with number of repetitions for A pattern, keeping constant the 300 mm/s speed and 30 kHz frequency.

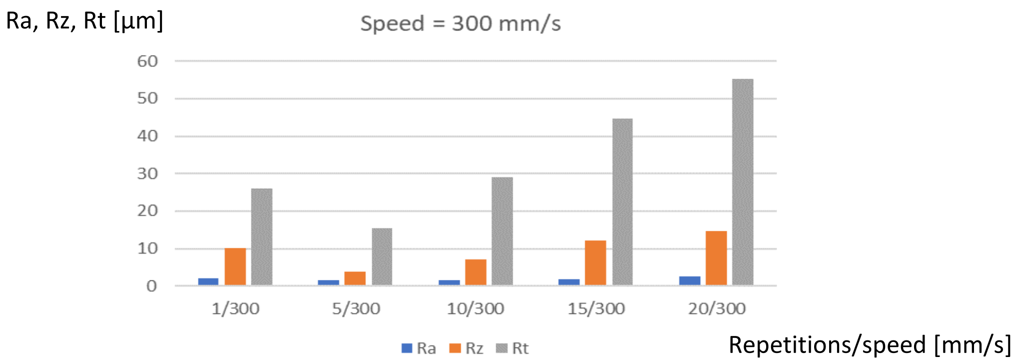

Figure 5.2. Surface roughness for design type A, speed 300 mm/s, frequency 30 kHz.

All the roughness parameters increase with increasing of the repetitions number. Figure 5.3 presents the variation of roughness parameters with the speed for A pattern, keeping constant the number of repetitions. The roughness parameters decrease with increasing of the speed.

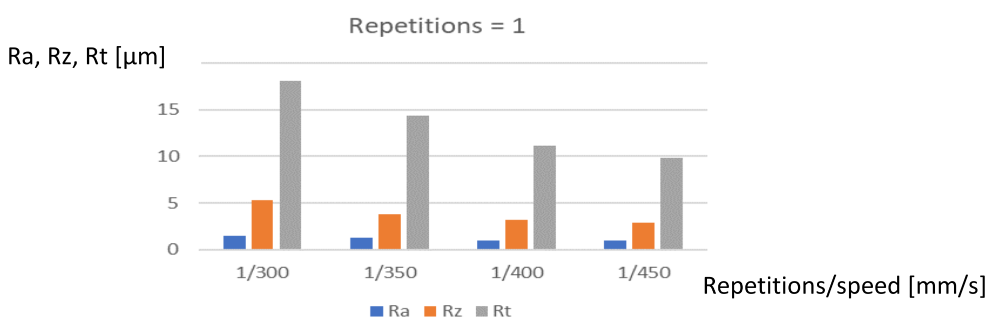

Figure 5.3. Surface roughness for design type A, one repetition.

5.1.2. Design type B, ellipses at 90° pattern

Overall, the results for surface roughness of ellipse pattern (Figure 5.4) are lower than the results from octagonal pattern, with an uneven trend. The values for roughness measurements once it grows, once it decreases, when the variable parameters are changed.

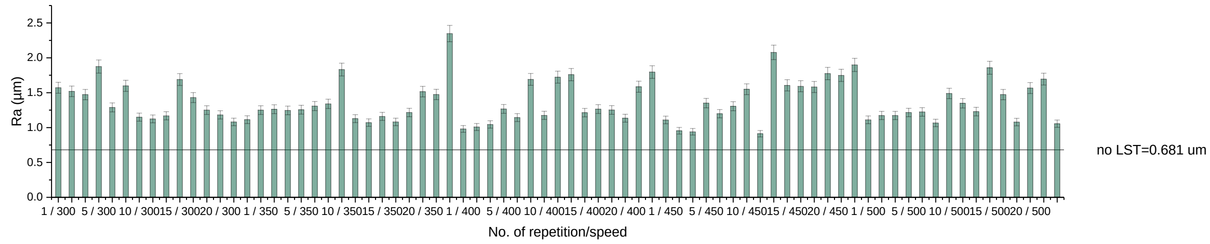

(a)

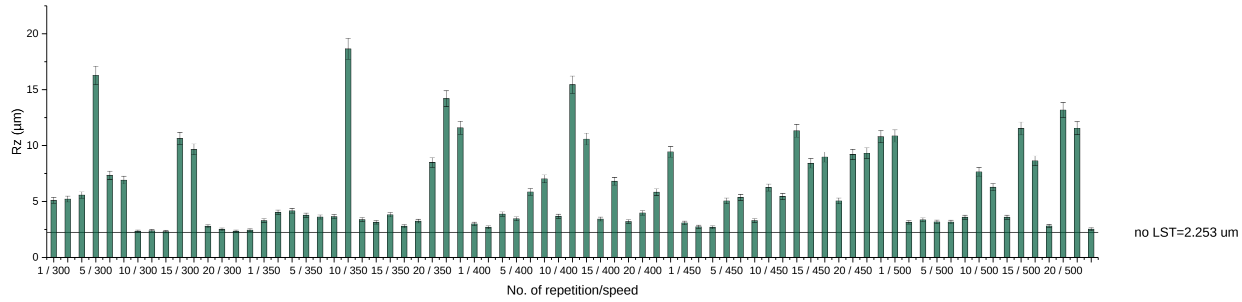

(b)

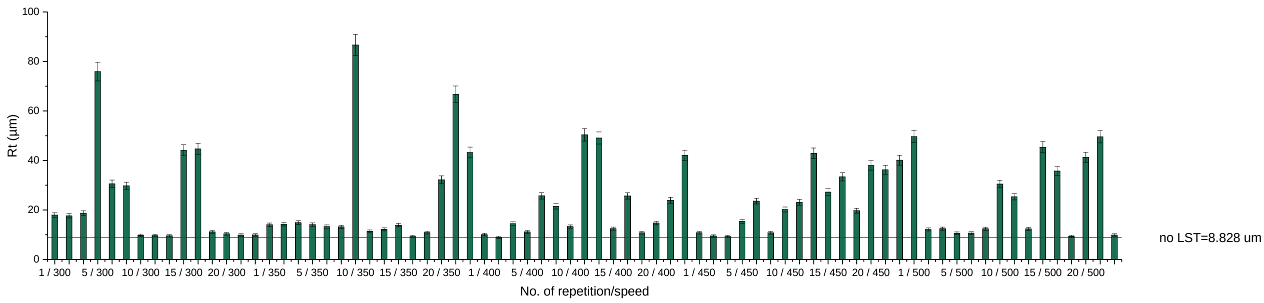

(c)

Figure 5.4. Surface roughness charts for design type B, R_a — arithmetical mean deviation of profile (a), R_z — total peak-to-valley- height (b) and R_t — ten-point height of irregularities (c).

5.1.3. Design type C, dimple/hole/crater array pattern

The image of all results (Figure 5.5), for design type C, is a maintaining trend for roughness. Out of this trend there are the roughness obtained for samples with 15 repetitions for 30 kHz and 300 mm/s speed, 10 repetitions for 40 kHz and 400 mm/s speed and 10 repetitions in the case of 60 kHz and 600 mm/s speed.

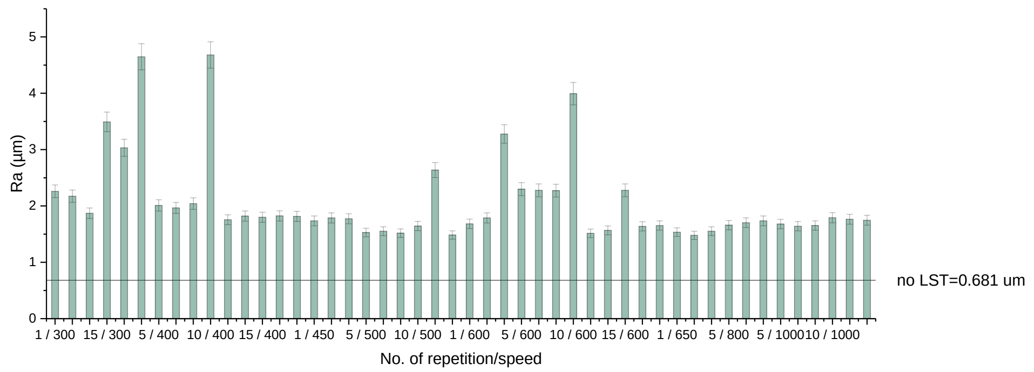

(a)

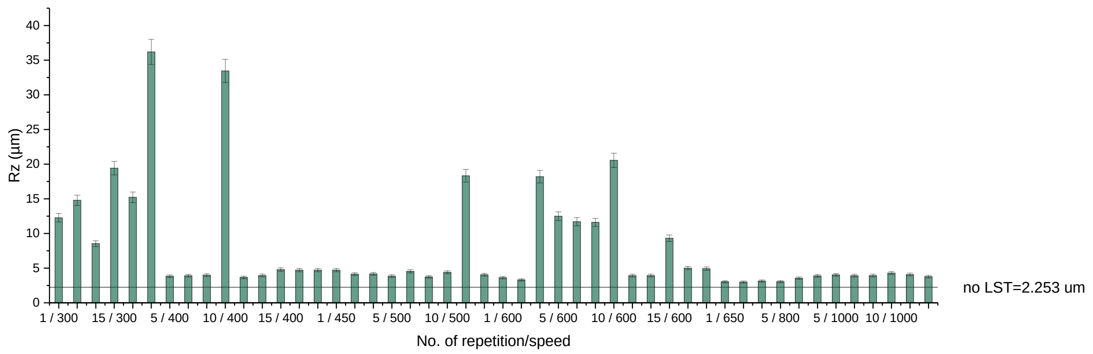

(b)

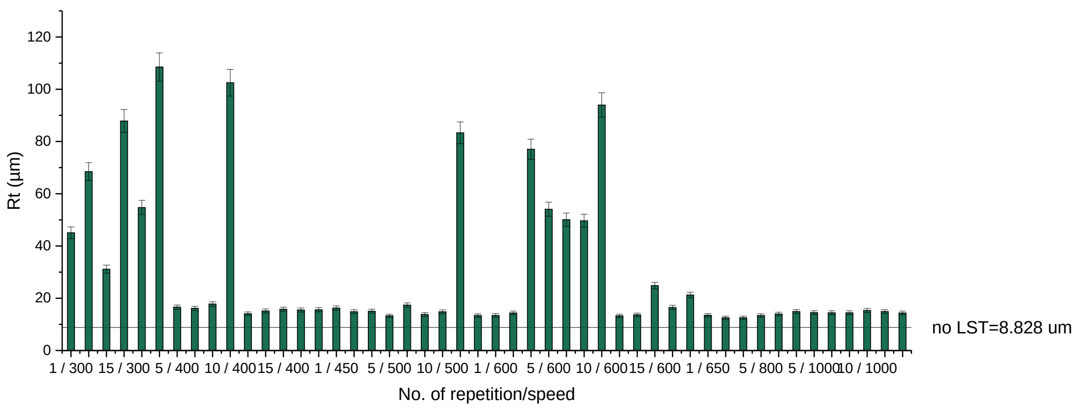

(c)

Figure 5.5. Surface roughness charts for design type C, R_a — arithmetical mean deviation of profile (a), R_z — total peak-to-valley- height (b) and R_t — ten-point height of irregularities (c).

5.2. Conclusions

The total height of the profile (R_t) between the lowest depth and the highest peak may indicate the difference between a sample that has recast from the ejected material and a sample that does not. In the diagram containing the results of the surface roughness for the type A pattern, it can be seen that when the number of repetitions is low, the height of the material expelled as recast material or burrs is low

As the number of repetitions of the laser beam transition increases, the height of the pull-out material increases. The difference between the average height and the total height of the profile is the depth of the crack and can be easily perceived from the diagrams (Figure 5.1), which applies to A pattern design.

Surface roughness has an important influence on function, strength, durability, and production cost. It was observed that the roughness of the textured surface is directly proportional to the spot density (number of repetitions), while roughness is inversely proportional to the processing speed. Since the density of the spot in the speed direction also decreases with increasing speed, it can be concluded that the roughness increases in value with increasing of spot no./cm^2.

The micro-texturing pattern applied also has an influence on the surface roughness. For a speed of 300 mm/s and a frequency of 30 kHz for a single pass, design type A provides the mean value of the measured surface roughness (R_a = 2.165 μm), being 1.4 times greater than mean value of design type B (R_a = 1.521 μm), and 1.03 times greater than mean value of design type C (R_a = 2.101 μm). Figures 5.1–5.3 show that the total height of the roughness profiles (R_t) reaches 28.963 μm for pattern A (10 repetitions/speed 300 mm/s) (Figure 5.1.c.), 9.633 μm for pattern B (10 repetitions/speed 300 mm/s) (Figure 5.2.c.) and 83.681 μm for pattern C (15 repetitions/speed 300 mm/s) (Figure 5.3.c.). The measures for (R_a), the arithmetic mean of the absolute values, on the whole surface reach 1.733 μm for pattern A (20 repetitions/speed 350 mm/s) (Figure 5.1.a), 1.779 μm for pattern B (20 repetitions/speed 350 mm/s) (Figure 5.2.a.) and 3.724 μm for pattern C (15 repetitions/speed 300 mm/s) (Figure 5.3.a.). The average roughness depth (R_z) reaches 9.501 μm for pattern A (20 repetitions/speed 350 mm/s) (Figure 5.1.b.), 8.393 μm pattern B (10 repetitions/speed 350 mm/s) (Figure 5.2.b), and 23.610 μm for pattern C (15 repetitions/speed 300 mm/s) (Figure 5.3.b.).

The results for surface roughness obtained for octagonal pattern, design type A, are increasing with increased number of repetitions and decrease with the speed value. The results for surface roughness of ellipse pattern, design type B, presents an uneven trend. The values for roughness measurements are increasing and decreasing, when the parameters (frequency, speed, number of repetitions) are changed. For dimple/hole/crater array pattern, design type C, is a maintaining trend for surface roughness results. All the three geometric shapes applied as LST patterns present an increase in roughness compared to the non-textured surface.

Surface functionalization by the fine modification of the roughness of the stainless steel finds its applicability in the industry. Type A microtextured design can be easily applied to the joining of different materials due to an uneven surface and an increased contact area. In tribological applications, recast material can be an impediment, but the joining of different materials requires this increase in contact area. The Type C model is mainly suitable for tribological applications due to the lack of recast material.

6. Wettability analysis of Laser Surface Texturing of AISI 430 Stainless Steel

The testing method applied to measure the contact angle is known as 'static' or even 'sessile drop', since on many surfaces the droplet remains static (the droplet often changes its dimensions with time, due to wetting phenomena) and in equilibrium with the material surface and air, according to ISO/TS 14778:2021. The static contact angle is measured from the baseline (material's surface) formed by means of a tangent on the droplet contour through one of the three-phase points at the specified contact time (or resulting from an average of measurements, for each time frame). The SCA lower than 20° is showing a super hydrophilic surface, less than 90° is considered hydrophilic surface, higher than 90° but lower than 150° is hydrophobic and over 150° is considered superhydrophobic.

6.1. Results and discussion

The base material (AISI 430 ferritic stainless steel), delivered in bright annealed conditions, has the mean static contact angle of 42.81°, measured according to the procedure presented in chapter 3.7.

Figure 6.1. Average static contact angle of the ferritic stainless steel without LST.

6.1.1. Design type A, octagonal donuts pattern

Figures 6.2 ...6.5 show the results of static contact angle measurements of design type A LST applied on AISI 430 samples, using different processing parameters. The increase of the static contact angle can be noticed, most of the times more than 90°, revealing a hydrophobic surface resulted after LST.

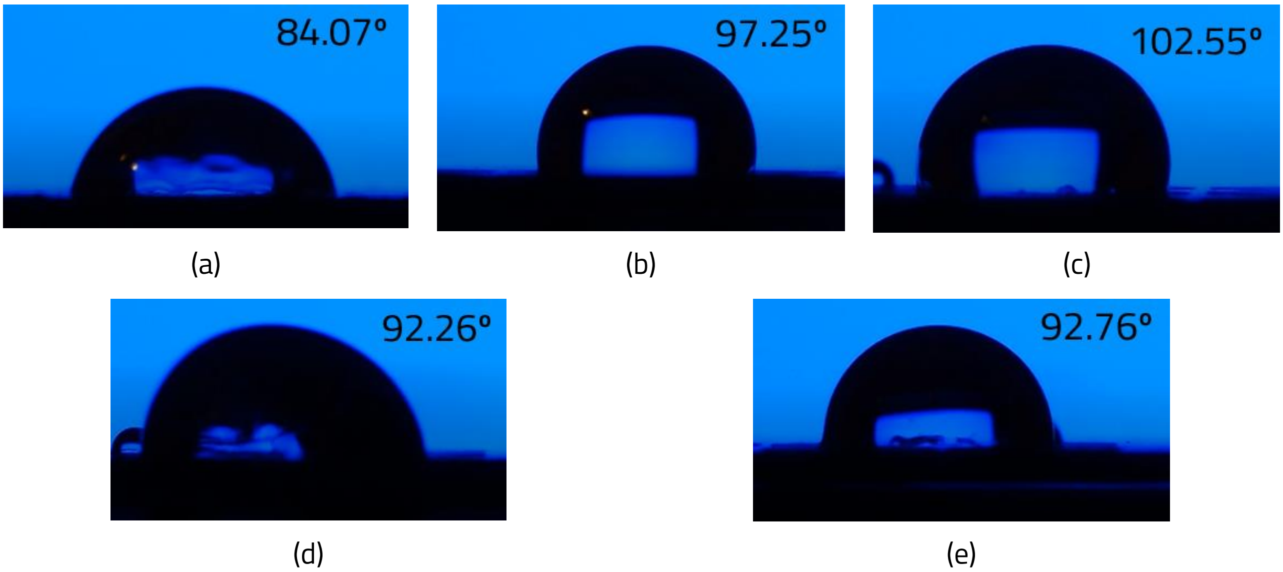

Figure 6.2. Images of the static contact angle measurement, 30 kHz frequency, 300 mm/s speed, no. of repetitions 1(a), 5(b), 10(c), 15(d) and 20(e).

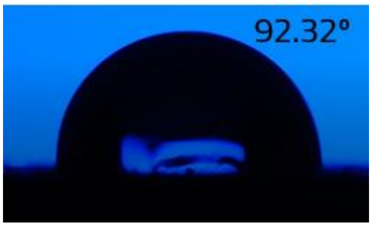

Figure 6.3. Image of the static contact angle measurement, frequency 35 kHz, speed 350 mm/s, no. of repetitions 20.

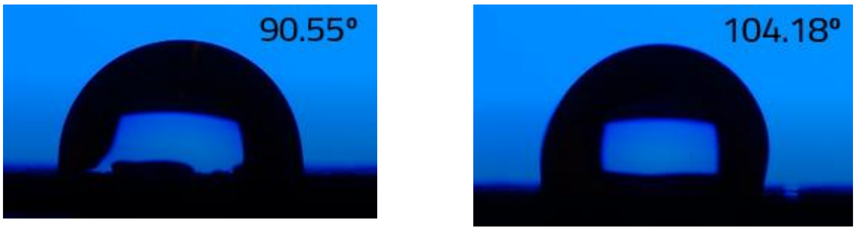

(a) (b)

Figure 6.4. Images of the static contact angle measurement, frequency 40 kHz, speed 400 mm/s, no. of repetitions 10 (a) and 20 (b).

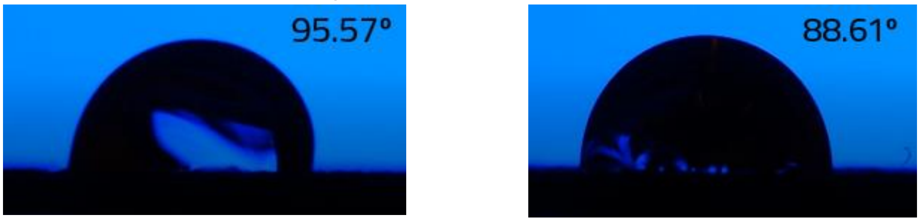

(a) (b)

Figure 6.5. Images of the static contact angle measurement, frequency 45 kHz, speed 450 mm/s, no. of repetitions 5 (a) and 20 (b).

Summarizing the results of the static contact angle measurements applied to the LST type A design, the graph in Figure 6.6 can be drawn.

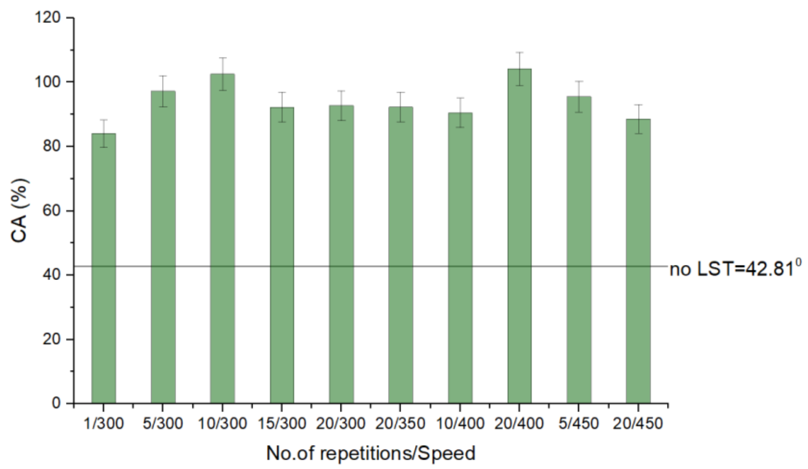

Figure 6.6. Average static contact angle for octagonal donuts pattern, design type A.

6.1.2. Design type B, ellipses at 90° pattern

Figures 6.7 ...6.11 show the results of static contact angle measurements of design type B LST applied on AISI 430 samples, using different processing parameters. There is an increasing in the static contact angle compared to the original, untextured surface.

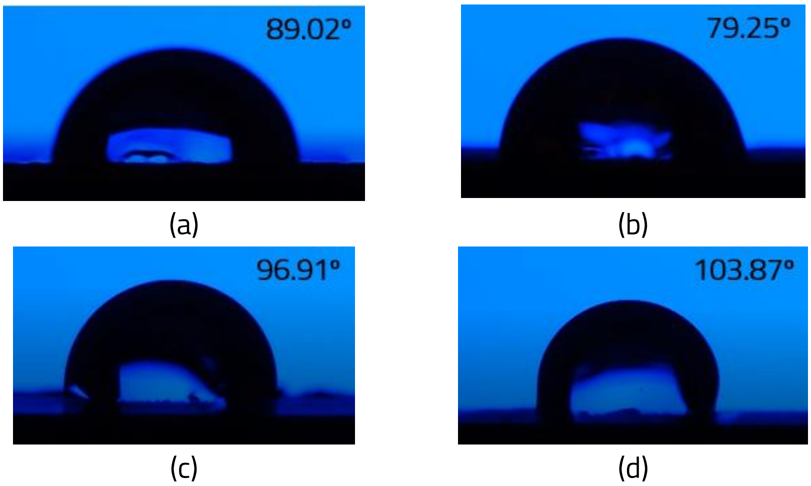

Figure 6.7. Images of the static contact angle measurement, frequency 30 kHz, speed 300 mm/s, no. of repetitions 1 (a), 5 (b), 10 (c) and 20 (d).

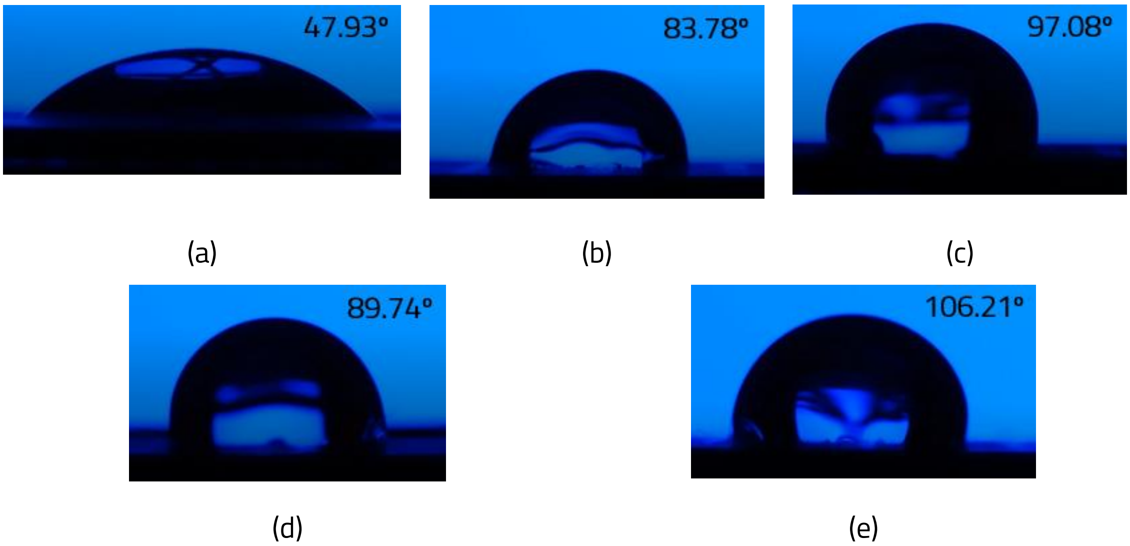

Figure 6.8. Images of the static contact angle measurement, frequency 40 kHz, speed 400 mm/s, no. of repetitions 1(a), 5(b), 10(c), 15(d) and 20(e).

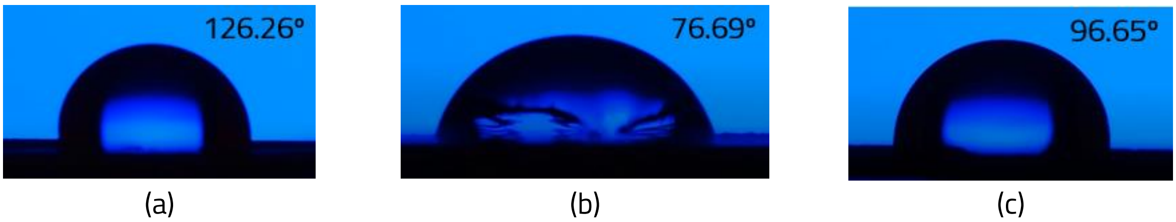

Figure 6.9. Images of the static contact angle measurement, frequency 50 kHz, speed 500 mm/s, no. of repetitions 10(a), 15(b) and 20(c).

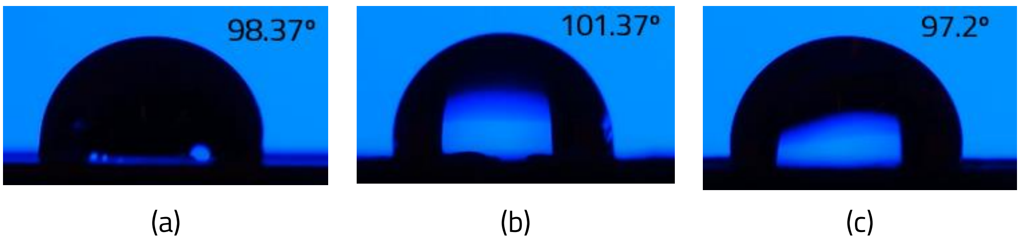

Figure 6.10. Images of the static contact angle measurement, frequency 65 kHz, speed 650 mm/s, no. of repetitions 1(a), 5(b), 10(c), 15(d) and 20(e).

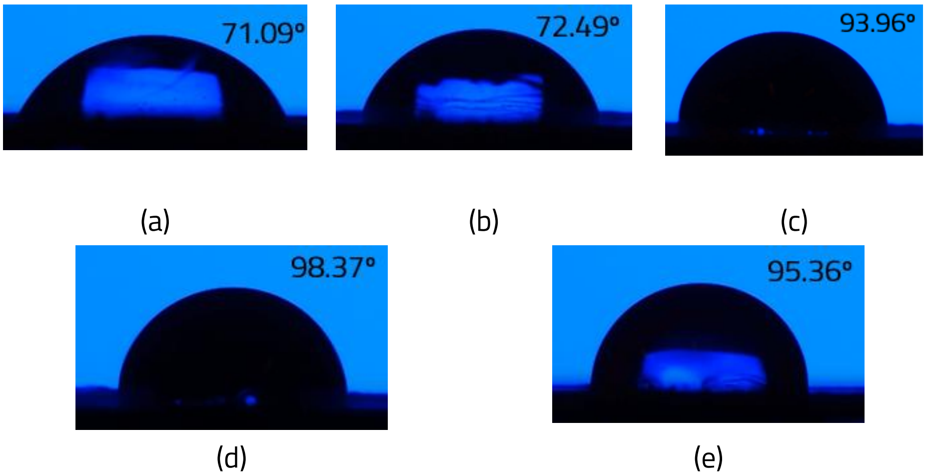

Figure 6.11. Images of the static contact angle measurement, frequency 100 kHz, speed 1000 mm/s, no. of repetitions 1(a), 5(b), 10(c), 15(d) and 20(e).

Summarizing the results of the static contact angle measurements applied to the LST type B design, the graph in Figure 6.12 can be drawn, thus demonstrating the increase of the hydrophobic character of the surface.

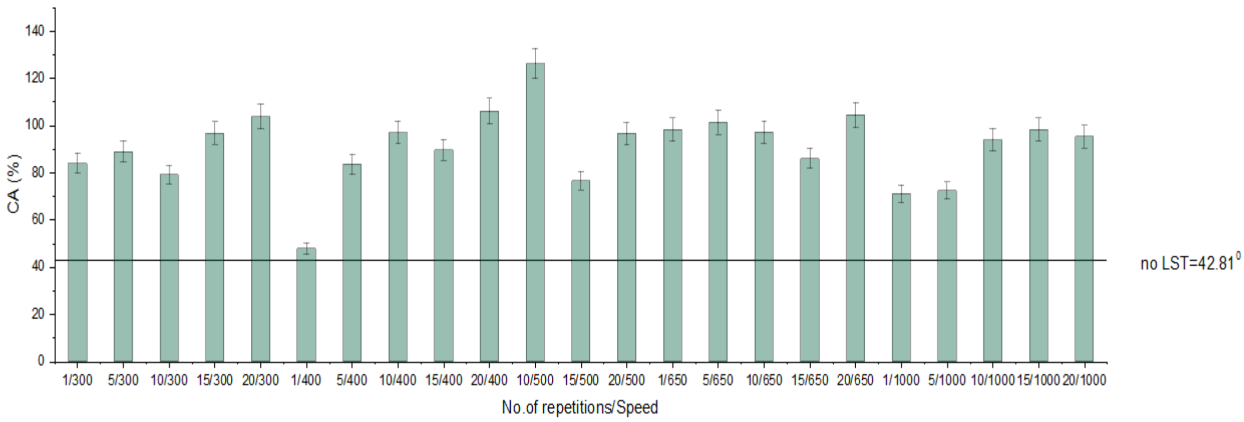

Figure 6.12. Average static contact angle for ellipse at 90° pattern, design type B.

Figure 6.13. and Figure 6.14. shows two deviations from the trend presented in Figure 6.12, increasing hydrophobicity with increasing number of repetitions. There is evidence of a deviation from the trend for the pattern type B (samples with 1 repetition and 10 repetitions for frequency of 40 kHz), where the drop of distilled water spreads very quickly, having a wetting behavior with high hydrophilicity. The very rapid spread (after three seconds) of the distilled water drop and the high wetting rate from hydrophobic to hydrophilic are noteworthy. The result of the static contact angle

measurements for pattern type B (1 repetition/frequency 40 kHz) cannot be measured by the equipment, because the microstructures belong to the extreme superhydrophilicity zone ($\theta = 0° \div 20°$).

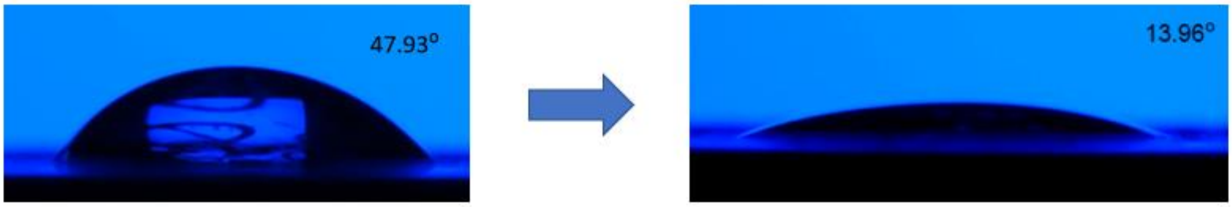

Figure 6.13. Aberration in static contact angle measurement of the sample design type B (no. of repetition 1/ frequency 40 kHz).

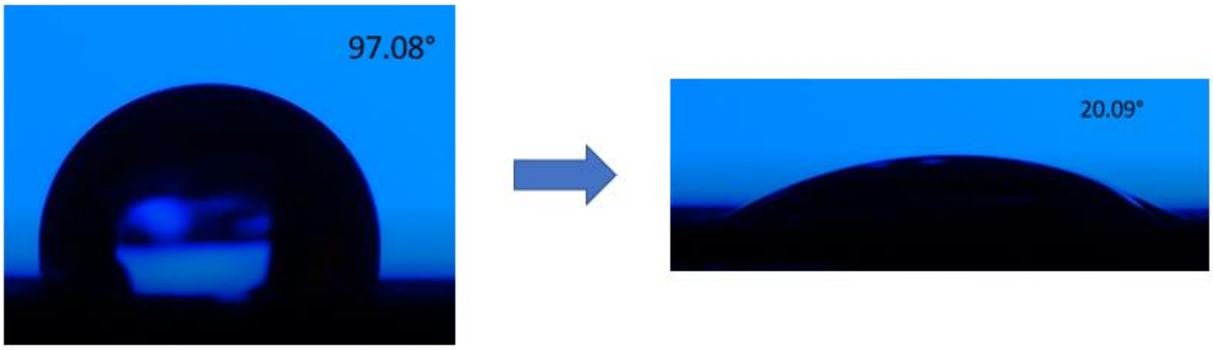

Figure 6.14. Aberration in static contact angle measurement of the sample design type B (no. of repetition 10/ frequency 40 kHz).

6.1.3. Design type C, dimple/hole/crater array pattern

Figures 6.15 ...6.20 show the results of static contact angle measurements of design type C LST applied on AISI 430 samples, using different processing parameters. Although the static contact angles measured in the case of type C design are smaller than in the previous two cases, the hydrophobicity compared to the original untextured material has increased.

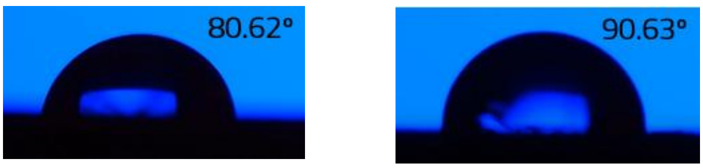

(a) (b)

Figure 6.15. Images of the static contact angle measurement, frequency 30 kHz, speed 300 mm/s, no. of repetitions 5(a) and 15(b).

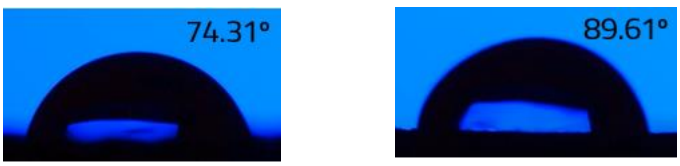

(a) (b)

Figure 6.16. Images of the static contact angle measurement, frequency 40 kHz, speed 400 mm/s, no. of repetitions 5(a) and 10(b).

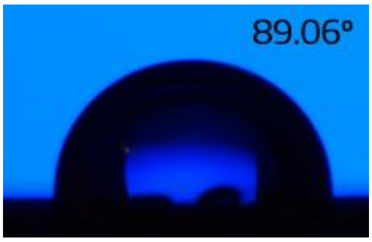

Figure 6.17. Image of the static contact angle measurement, frequency 45 kHz, speed 450 mm/s, 1 repetition.

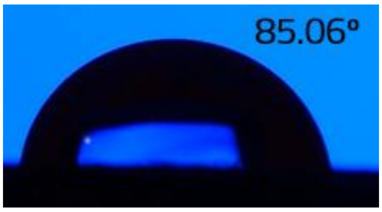

Figure 6.18. Image of the static contact angle measurement, frequency 50 kHz, speed 500 mm/s, 5 repetitions.

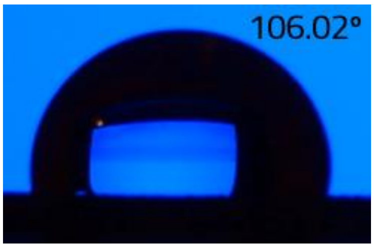

Figure 6.19. Image of the static contact angle measurement, frequency 60 kHz, speed 600 mm/s, 1 repetition.

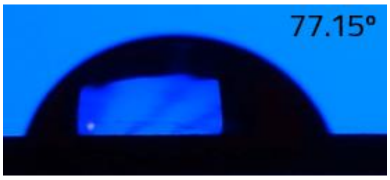

Figure 6.20. Image of the static contact angle measurement, frequency 80 kHz, speed 800 mm/s, 15 repetitions.

Figure 6.21 shows the change in static contact angles measured with the processing parameters for the design of LST type C.

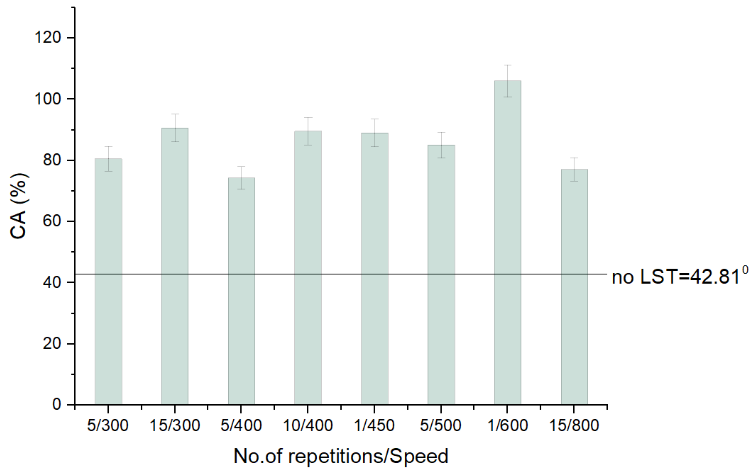

Figure 6.21. Average static contact angle for dimple/hole/crater array pattern, design type C.

6.2. Conclusions

All patterns' designs applied as texturing on the surface of ferritic stainless steel by nanosecond pulsed indicate an improvement in the average static contact angle of the base material. Given the graph in Figure 6.6, the results for pattern type A, average static contact angle have a constancy, and most of the results show a hydrophobicity. For pattern type B (Figure 6.12), the best result in terms of hydrophobicity involves at least 20 repetitions. When less than 20 repetitions were used on the textured pattern B, hydrophilicity was obtained. Surprisingly, for pattern type C (Figure 6.21), the rule that applies is contrary to the other two design types of textured patterns in terms of the number of repetitions of passages. As the repetitions of the micro-textured patterns increases, a slight decrease in the average static contact angle can be observed. Another notable influence on the result of the average static contact angle is the frequency. For lower than 40 kHz frequency (applicable for designs type B and C), the average static contact angle does not exceed 90°.

The repeatability of the laser beam passage has a strong influence on static contact angle. For low number of repetitions, the static contact angle is less than 90°, indicating hydrophilicity. The influence of the textured pattern indicates an improvement (the average static contact angle is double that of the base material). It has been determined that the static contact angle increases at a higher fluency, mainly because the fluency is proportional to the repetition rate.

The results of the wettability analysis of LST areas provide an insight into the influence of the number of repetitions and the frequency. As the number of repetitions increases, keeping the frequency constant, the measured static contact angle increases, providing hydrophobicity to the surface of the microstructure, and a decrease in static contact angle values occurs as the frequency increases and the number of repetitions is constant. For 400 mm/s speed, at 40 kHz frequency and 10 repetitions, and pattern A (CA = 90.55°) and pattern B (CA = 97.08°), the wettability measurement provides hydrophobic surfaces (CA > 90°). The results for 400 mm/s speed, at 40 kHz frequency and 10 repetitions with pattern C are at the limit of hydrophobicity (CA = 89.61°), but with a remarkably improving of CA value compared to the base material without LST (CA = 42.81°). The recast material and the groove depth of the patterns also have a significant influence on the static contact angle. The increase in roughness due to the texture of the surface increases the static contact angle with values between 30 and 195% higher than for the untextured surface, thus increasing the hydrophobicity.

7. Final conclusions. Original contributions. Dissemination of results. Further research

The patterns designs and geometries were chosen based on creating a connection with the previous literature, and to offer a better approach for simple automatization, wide applicability, and fast transition in flow-production. The motivation was to offer a pattern which can be applied in LST for tribological applications, joining dissimilar materials and bioengineering.
The results of the experimental research presented is leading to the following conclusions:

- Cross section and top view optical micrographs with profile histograms are offering information regarding the material displacement after LST, evaporated and/or deposited in the form of recast material and splashes. Comparing the design patterns, the octagonal donuts (design type A) and dimple/hole/crater array (design type C) patterns have more pronounced displacements towards ellipses at 90° (design type B) pattern. The design type A have the higher values of recast material and design type C have the high number of splashes. The design type B has in its composition both, recast material and splashes, but with much lower values than the other two patterns. The microscopic images also show the thermally influenced area, the appearance of chromium oxide and the phenomenon of imperfect trajectory.
- The SEM images (top view and cross section) offers information about the phenomena that occur during LST, patterns present a low area of recast material (design type C) and splashes (design type A). The SEM and EDX analysis are outlining the presence of the oxygen, which is beneficial for the ferritic stainless steel by creating an oxide layer (passive layer). The recast material is showing the double value for the carbon element for octagonal donuts pattern. The analysis in the thermally affected area is pointing appropriate elemental analysis for all patterns. EDX analysis offers the answer regarding the micro textured area, that nothing changed.
- Regarding the surface roughness analysis, the results are showing that pattern design A have an increased values of roughness while the parameters (fluence and number of repetitions) increase. The pattern design type B present an uneven trend, while pattern design type C is maintaining trend. All the three geometric shapes applied as LST patterns present an increase in roughness, but the octagonal donuts pattern offers the best outcome regarding surface roughness. The microtextured design type A can be easily applied in joining dissimilar materials due to an irregular surface and an increased contact area. In tribological applications, recast material can be an impediment, but in the joining of dissimilar materials, this increasing of the contact area is required. The pattern design type C is suitable mainly for tribological applications since the recast material is missing. In the case of pattern design type B, more future research is needed, as the results offers uneven results. Due to the irregular surface and increased contact area, the A-type micro textured pattern can be easily used to join dissimilar materials. In tribological applications, the expulsed material can be a hindrance, but the increased contact area is necessary when joining dissimilar materials. Pattern C design is recommended, mainly, for tribological applications due to lack of recast material. In the case of pattern design type B, more future research is needed, as the results offers uneven results.
- All samples where LST was applied to the ferritic stainless-steel surface, micro texturing showed an improvement in the average static contact angle of the surface. When the number

of repetitions is low, the static contact angle is less than 90°, indicating hydrophilicity. It has been found that the static contact angle increases with higher fluence, mainly because the fluence is proportional to the repetition rate. The recast material and gap depth of the samples also had a significant effect on the static contact angle. The increased surface roughness due to surface micro texturing increases the static contact angle, which is 30% to 195% higher than the bare substrate, thereby increasing hydrophobicity.

- It has been noticed that roughness of a micro textured surface is proportional to the point density (number of iterations) and inversely proportional to the processing speed. When the expulsed material is present in abundance (pattern A), a surface with high roughness is obtained because the overlap is higher and high crack depths are recorded in the pattern without overlap and recast material, as in pattern type C. Design B has a lower level of overlap and thus obtains intermediate values of surface roughness. Fine setup of the roughness of stainless-steel has many industrial applications, especially in bioengineering, and dissimilar joining.
- Morphological analysis provides valuable information about the microrelief of laser textured surfaces, clues for mechanical interlocking in the case of hybrid joints. Of the three patterns analysed, the highest level of recast material is observed for design type A, being more recommended its application for the preparation of the metal surface before hybrid welding.

I consider that this doctoral thesis brings the following original contributions:

- Microtextures were made using a cheap industrial nanosecond pulsed laser, creating two new design patterns: 3 octagonal concentric donuts and 2 ellipses at 90° closed loops, and one used by other researchers (dimple/hole/crater array), for comparison.
- The influence of the pattern and of the LST parameters on the surface roughness was demonstrated, all the tested patterns conferring an increased roughness compared to the non-textured material.
- The influence of the microstructuring pattern and of the LST parameters on the wettability tuning was highlighted, most of the patterns and processing parameters used are offering hydrophobic surfaces (SCA> 90°), except for the pattern design type C, where the hydrophilic character predominates.
- Recommendations for different applications design and industrial manufacturing based on research results were provided.

Published papers during doctoral studies:

1. Moldovan, E.; Tierean, M.H.; Stanciu, E.M. Overview of Joining Dissimilar Materials: Metals and Polymers. *Bulletin of Transilvania Univ.* **2017**, *10(1),* 39-46.
2. Moldovan, E.R.; Concheso Doria, C.; Ocaña Moreno, J.L.; Baltes, L.S.; Stanciu, E.M.; Croitoru, C.; Pascu, A.; Tierean, M.H. Geometry Characterization of AISI 430 Stainless Steel Microstructuring Using Laser. *Archives of Metallurgy and Materials* **2022,** *67,* 645–652 (IF=0.767).
3. Moldovan, E.R.; Concheso Doria, C.; Ocaña, J.L.; Baltes, L.S.; Stanciu, E.M.; Croitoru, C.; Pascu, A.; Roata, I.C.; Tierean, M.H. Wettability and Surface Roughness Analysis of Laser Surface Texturing of AISI 430 Stainless Steel. *Materials* **2022,** *15,* 2955 (IF=3.623).
4. Moldovan, E.R.; Concheso Doria, C.; Ocaña, J.L.; Istrate, B.; Cimpoesu, N.; Baltes, L.S.; Stanciu, E.M.; Croitoru, C.; Pascu, A.; Munteanu, C.; Tierean, M.H. Morphological Analysis of Laser Surface Texturing Effect on AISI 430 Stainless Steel. *Materials* **2022**, *15*, 4580 (IF=3.623).

Subsequent investigations will be performed to obtain super hydrophobic surfaces using design type B optimized by decreasing the center-to-center distance of the micro-texturing pattern. To identify the effect of LST on the stainless character of AISI 430 steel, by future research that will include X-ray diffraction and corrosion studies. The next step is to research the octagonal and ellipse pattern design for hybrid joints, and dimple/hole/crater array pattern design in tribological applications.

References

2 Ahmed, Y.S.; DePaiva, J.M.; Amorim, F.L.; Torres, R.D.; De Rossi, W.; Veldhuis, S.C. Laser surface texturing and characterization of austenitic stainless steel for the improvement of its surface properties. *Int. J. Adv. Manuf. Technol*. **2021**, *115*, 1795–1808.

8 Cardoso, J.T.; Aguilar-Morales, A.I.; Alamri, S.; Huerta-Murillo, D.; Cordovilla, F.; Lasagni, A.C.; Ocaña, J.L. Superhydrophobicity on hierarchical periodic surface structures fabricated via direct laser writing and direct laser interference patterning on an aluminium alloy, *Optics and Lasers in Eng*. **2018**, *111,* 193-200.

10 Carvalho, A.; Grenho, L.; Fernandes, M.H.; Daskalova, A.; Trifonov, A.; Buchvarov, I.; Monteiro, F.J. Femtosecond laser microstructuring of alumina toughened zirconia for surface functionalization of dental implants, *Ceram. Int.* **2020**, *46(2)*, 1383-1389.

15 Collins, C.M.; Safiuddin, M. Lotus-Leaf-Inspired Biomimetic Coatings: Different Types, Key Properties, and Applications in Infrastructures. *Infrastructures* **2022**, *7*, 46.

16 Costa, H.L.; Schille, J.; Rosenkranz, A. Tailored surface textures to increase friction-A review. *Friction* **2022**, https://doi.org/10.1007/s40544-021-0589-y.

17 Cruz-Ramírez, A.; Sánchez-Olvera, R.; Zamarrón-Hernández, D.; Hautefeuille, M.; Cabriales, L.; Jiménez-Díaz, E.; Díaz-Bello, B.; López-Aparicio, J.; Pérez-Calixto, D.; Cano-Jorge, M.; Vázquez-Victorio, G. Progress on the Use of Commercial Digital Optical Disc Units for Low-Power Laser Micromachining in Biomedical Applications. *Micromachines* **2018**, *9*, 187.

18 Cui, X.; Li, Y.; Guo, J.; Ming, P. Effects of bio-inspired integration of laser-induced microstructure and coated cemented carbide on tool performance in green intermittent turning*. J. Manuf. Process.* **2021**, *65*, 228–244.

20 Czotscher, T.; Vollertsen, F. Analysis of melting and melt expulsion during pulsed laser ablation. *Physcs. Proc.* **2016**, *83*, 53-61.

21 Daskalova, A.; Bliznakova, I.; Angelova, L.; Trifonov, A.; Declercq, H.; Buchvarov, I. Femtosecond Laser Fabrication of Engineered Functional Surfaces Based on Biodegradable Polymer and Biopolymer/Ceramic Composite Thin Films. *Polymers* **2019**, *11*, 378.

23 De Zanet, A.; Casalegno, V.; Salvo, M. Laser surface texturing of ceramics and ceramic composite materials – A review. *Ceram. Int.* **2021**, *47*, 7307-7320.

27 Feng, Y.; Gao, X.; Zhang, Y.; Peng, C.; Gui, X.; Sun, Y.; Xiao, X. Simulation and experiment for dynamics of laser welding keyhole and molten pool at different penetration status. *Int. J. Adv. Manuf. Technol.* **2021**, *112*, 2301-2312.

32 Ge, C.; Yuan, G.; Guo, C.; Ngo, C.V.; Li, W. Femtosecond laser fabrication of square pillars integrated Siberian-Cocklebur-like microstructures surface for anti-icing. *Mater. Des.* **2021**, *204*, 109689.

33 Geyer, F.; D'Acunzi, M.; Sharifi-Aghili, A.; Saal, A.; Gao, N.; Kaltbeitzel, A.; Sloot, T.F.; Berger,

R.; Butt, H.J.; Vollmer, D. When and how self-cleaning of superhydrophobic surfaces works. *Sci. Adv.* **2020**, *6*, eaaw9727.

34 Giorleo, L.; Montesano, L.; La Vecchia, G.M. Laser Surface Texturing to Realize Micro grids on DLC Coating: Efect of Marking Speed, Power, and Loop Cycle. *Int. J. Precis. Eng.* **2021**, *22*, 745–758.

36 Gregorčič, P.; Conradi, M.; Hribar, L.; Hočevar, M. Long-Term Influence of Laser-Processing Parameters on (Super)hydrophobicity Development and Stability of Stainless-Steel Surfaces. *Materials* **2018**, *11*, 2240.

37 Grigoropoulos, C.P. Laser synthesis and functionalization of nanostructures. *Int. J. Extrem. Manuf.* **2019**, *1*, 012002.

39 Guimarães, B.; Fernandes, C.M.; Figueiredo, D.; Carvalho, O.; Silva, F.S.; Miranda, G. Effect of laser surface texturing on the wettability of WC-Co cutting tools. *Int. J. Adv. Manuf. Technol.* **2020**, *111*, 1991–1999.

41 Hsu, C.J.; Stratmann, A.; Medina, S.; Jacob, G.; Mücklich, F.; Gachot, C. Does laser surface texturing really have a negative impact on the fatigue lifetime of mechanical components? *Friction* **2021**, *9*, 1766–1775.

42 Hu, G.; Guan, K.; Lu, L.; Zhang, J.; Lu, N.; Guan, Y. Engineered Functional Surfaces by Laser Microprocessing for Biomedical Applications. *Engineering* **2018**, *4(6),* 822-830.

43 Hu, G.; Song, Y.; Guan, Y. Tailoring metallic surface properties induced by laser surface processing for industrial applications, *Nanotechnol Precis Eng.* **2019**, *2(1),* 29-34.

46 Jalil, S.A.; Akram, M.; Bhat, J.A.; Hayes, J.J.; Singh, S.C.; ElKabbash, M.; Guo. C. Creating superhydrophobic and antibacterial surfaces on gold by femtosecond laser pulses. *Appl. Surf. Sci.* **2020**, *506*, 144952.

47 Jing, X.; Yang, C.; Zheng, S.; Chen, X.; Zhao, Y. Investigation of Wettability of Zirconia by Nanosecond Laser Treatment. *Proceedings of the IEEE International Conference on Manipulation, Manufacturing and Measurement on the Nanoscale* (3M-NANO), Hangzhou, China, 13–17 August **2018**.

50 Kanidia, M.; Papagiannopoulos, A.; Matei, A.; Dinescu, M.; Pispas, S.; Kandyla, M. Functional surfaces of laser-microstructured silicon coated with thermoresponsive PS/PNIPAM polymer blends: Switching reversibly between hydrophilicity and hydrophobicity. *Appl. Surf. Sci.* **2020**, *527*, 146841.

51 Karapanagiotis, I. Water- and Oil-Repellent Surfaces. *Coatings* **2020**, *10*, 920.

60 Lambiase, F.; Scipioni, S.I.; Lee, C.J.; Ko, D.C.; Liu, F. A State-of-the-Art Review on Advanced Joining Processes for Metal-Composite and Metal-Polymer Hybrid Structures. *Materials* **2021**, *14*, 1890.

61 Li, J.; Zhu, R.; Huang, Y. Fabrication of microstructures by picosecond laser. *Optik* **2021**, *232*, 166501.

63 Li, X.; Jiang, Y.; Zhang, Z.; Jiang, Z.; Lian, J.; Ren, L. Facile and environmentally friendly fabrication of underwater superaerophobic and superaerophilic metallic surfaces through laser ablation and heat treatment. *Colloids Surf. A Physicochem. Eng. Asp.* **2021**, *621*, 126547.

64 Liang, Y.; Zhao, J.; Yan, S. Honeybees have Hydrophobic Wings that Enable Them to Fly

through Fog and Dew, *J. Bionic Eng.* **2017**, *14(3),* 549-556.

66 Lin, W.H.; Chen, C.W.; Wang, S.H.; Li, B.R. Rapid construct superhydrophobic microcracks on the open-surface platform for droplet manipulations. *Sci. Rep.* **2021**, *11*, 14915.

68 Liu, W.; Liu, S.; Wang, L. Surface Modification of Biomedical Titanium Alloy: Micromorphology, Microstructure Evolution and Biomedical Applications. *Coatings* **2019,** *9(4),* 249.

71 Matta, A.; Sedlacek, T.; Kadleckova, M.; Lengalova, A. The Effect of Surface Substrate Treatments on the Bonding Strength of Aluminium Inserts with Glass-Reinforced Poly(phenylene) Sulphide. *Materials* **2022**, *15*, 1929.

72 Milles, S.; Soldera, M.; Voisiat, B.; Lasagni, A.F. Fabrication of superhydrophobic and ice-repellent surfaces on pure alumium using single and multiscaled periodic textures. *Sci. Rep.* **2019**, *9*, 13944.

74 **Moldovan, E.; Tierean, M.H.; Stanciu, E.M. Overview of Joining Dissimilar Materials: Metals and Polymers.** ***B. Transilvania Univ.*** 2017, ***10(1),*** **39-46.**

75 **Moldovan, E.R.; Concheso Doria, C.; Ocaña Moreno, J.L.; Baltes, L.S.; Stanciu, E.M.; Croitoru, C.; Pascu, A.; Tierean, M.H. Geometry Characterization of AISI 430 Stainless Steel Microstructuring Using Laser.** ***Arch. Metall. Mater.*** 2022, ***67*****, 645–652.**

76 **Moldovan, E.R.; Concheso Doria, C.; Ocaña, J.L.; Baltes, L.S.; Stanciu, E.M.; Croitoru, C.; Pascu, A.; Roata, I.C.; Tierean, M.H. Wettability and Surface Roughness Analysis of Laser Surface Texturing of AISI 430 Stainless Steel.** ***Materials*** 2022, ***15*****, 2955.**

77 **Moldovan, E.R.; Concheso Doria, C.; Ocaña, J.L.; Istrate, B.; Cimpoesu, N.; Baltes, L.S.; Stanciu, E.M.; Croitoru, C.; Pascu, A.; Roata, I.C.; Tierean, M.H. Morphological Analysis of Laser Surface Texturing Effect on AISI 430 Stainless Steel.** ***Materials*** 2022, ***15*****, 4580.**

78 Moravčíková, J.; Moravčík, R.; Kusý, M.; Necpal, M. Influence of Laser Surface Texturing on Tribological Performance of Tool Steels. *J. Mater. Eng. Perform.* **2018**, *27*, 5417–5426.

80 Obilor, A.F.; Pacella, M.; Wilson, A.; Silberschmidt, V.V. Micro-texturing of polymer surfaces using lasers: a review. *Int. J. Adv. Manuf. Technol.* **2022**, *120*, 103–135.

81 Ocaña, J.L.; Jagdheesh, R.; García-Ballesteros, J.J. Direct generation of superhydrophobic microstructures in metals by UV laser sources in the nanosecond regime. *Adv. Opt. Technol.* **2016**, *5(1),* 87-93.

82 Ocaña, J.L.; Huerta-Murillo, D.; Lasagni, A.F.; Aguilar-Morales, A.I.; Alamri, S.; Cardoso, J.T.; García-Beltrán, A.; Cordovilla, F.; Angulo, I. Modification of Ti6Al4V surface properties by combined DLW-DLIP hierarchical micro-nano structuring, *Advanced Optical Technologies,* **2020**, *9(3),* 121-130.

83 Ortiz, R.; Aurrekoetxea-Rodríguez, I.; Rommel, M.; Quintana, I.; Vivanco, M.d.; Toca-Herrera, J.L. Laser Surface Microstructuring of a Bio-Resorbable Polymer to Anchor Stem Cells, Control Adipocyte Morphology, and Promote Osteogenesis. *Polymers* **2018**, *10*, 1337.

84 Palmieri, F.L.; Belcher, M.A.; Wohl, C.J.; Blohowiak, K.Y.; Connell, J.W. Laser ablation surface preparation for adhesive bonding of carbon fiber reinforced epoxy composites. *Int. J. Adhes. Adhes.* **2016**, *68*, 95-101.

85 Patel, D.; Jain, V.K.; Ramkumar, J. Micro texturing on metallic surfaces: State of the art. *Proc IMechE Part B: J Engineering Manufacture* **2016**, *232(6),* 1–24.

87 Puoza, J.C. Efect of Auxiliary Gas and Light Absorbing Coatings on Laser Surface Texturing. *Lasers Manuf. Mater. Process.* **2021**, *8*, 125–139.

88 Quintanilla-Correa, D.I.; Peña-Parás, L.; Maldonado-Cortés, D.; Rodriguez-Villalobos, M.C.; Hernández-Rodríguez, M.A.L. State of the art of surface texturing for biotribology applications, *Int. J. Adv. Manuf. Technol.* **2021**, *XIII(3)*, 143-150.

89 Rauh, S.; Wöbbeking, K.; Li, M.; Schade, W.; Hübner, E.G. From Femtosecond to Nanosecond Laser Microstructuring of Conical Aluminum Surfaces by Reactive Gas Assisted Laser Ablation. *Chem. Phys. Chem.* **2020**, *21*, 1644-1652.

91 Rodríguez-Vidal, E.; Sanz, C.; Lambarri, J.; Renard, J.; Gantchenko, V. Laser joining of different polymer-metal configurations: analysis of mechanical performance and failure mechanisms. *Physcs. Proc.* **2016**, *83*, 1110-1117.

92 Rodríguez-Vidal, E.; Sanz, C.; Soriano, C.; Leunda, J.; Verhaeghe, G.; Effect of metal micro-structuring on the mechanical behavior of polymer–metal laser T-joints. *J. Mater. Process. Technol.* **2016**, *229*, 668–677.

93 Rodríguez-Vidal, E.; Sanz, C.; Lambarri, J.; Quintana, I.; Experimental investigation into metal micro-patterning by laser on polymer-metal hybrid joining. *Opt. Laser Technol.* **2018**, *104*, 73–82.

95 Rupasov, A.E.; Danilov, P.A.; Kudryashov, S.I. Femtosecond-laser microstructuring in transparent materials. *J. Phys.: Conf. Ser.* **2020**, *1692*, 012011.

96 Salstela, J.; Suvanto, M.; Pakkanen, T.T. Influence of hierarchical micro-micro patterning and chemical modifications on adhesion between aluminum and epoxy. *Int. J. Adhes. Adhes.* **2016**, *66*, 128–137.

97 Samoila, C.; Ursutiu, D.; Tavkhelidze, A.; Jangidze, L.; Taliashvili, Z.; Skhiladze, G.; Tierean, M. Nanograting layers of Si. *Nanotechnology* **2020**, *31*, 035301.

98 Sanjay Raja, R.S.; Selvakumar, P.; Babu, P.D.; Rubasingh, B.J.; Suresh, K. Influence of laser parameters on superhydrophobicity—A review. *Eng. Res. Express* **2021**, *3*, 022001.

103 Schricker, K.; Samfaß, L.; Grätzel, M.; Ecke, G.; Bergmann, J.P. Bonding mechanisms in laser-assisted joining of metal-polymer composites. *J. Adv. Join. Process.* **2020**, *1*, 100008.

104 Sergeev, D.G.; Marinin, E.A.; Kokorin, V.V.; Anufriev, D.S. The improvement of surface quality characteristics after mechanical treatment by pulse laser radiation. *Mater. Today Proc.* **2021**, *38*, 1613–1616.

105 Setti, D.; Arrabiyeh, P.A.; Kirsch, B.; Heintz, M.; Aurich, J.C. Analytical and experimental investigations on the mechanisms of surface generation in micro grinding. *Int. J. Mach. Tools Manuf.* **2020**, *149*, 103489.

107 Shivakoti, I.; Kibria, G.; Cep, R.; Pradhan, B.B.; Sharma, A. Laser Surface Texturing for Biomedical Applications: A Review. *Coatings* **2021**, *11*, 124.

108 Singh, A.; Singh, D.; Ramkumar, J.; Balani, K. Single step laser surface texturing for enhancing contact angle and tribological properties. *Int. J. Adv. Manuf. Technol.* **2019**, *100*, 1253–1267.

109 Sirdeshmukh, N.; Dongre, G. Laser micro & nano surface texturing for enhancing osseointegration and antimicrobial effect of biomaterials: A review. *Mater. Today-Proc.* **2021**, *44*, 2348-2355.

111 Stanciu, E.M.; Păvălache, A.C.; Dumitru, G.M.; Dontu, O.G.; Besnea, D.; Vasile, I.M. Mechanism of keyhole formation in laser welding. *The Romanian Review Precision Mechanics, Optics & Mechatronics,* **2010,** *38(20),* 171-176.

114 Sun, L.; Guo, J.; Chen, H.; Zhang, D.; Shang, L.; Zhang, B.; Zhao, Y. Tailoring materials with specific wettability in biomedical engineering, *Adv. Sci.* **2021**, *8*, 2100126.

116 Ta, V.D.; Dunn, A.; Wasley, T.J.; Li, J.; Kay, R.W.; Stringer, J.; Smith, P.J.; Esenturk, E.; Connaughton, C.; Shephard, J.D. Laser textured superhydrophobic surfaces and their applications for homogeneous spot deposition. *Appl. Surf. Sci.* **2016**, *365*, 153–159.

118 Van der Straeten, K.; Burkhardt, I.; Olowinsky, A.; Gillner, A. Laser-induced Self-organizing Microstructures on Steel for Joining with Polymers. *Phys. Procedia* **2016**, *83*, 1137-1144.

119 Vermaj, J.; Taiwade, R.V. Effect of welding processes and conditions on the microstructure, mechanical properties and corrosion resistance of duplex stainless steel weldments-a review, *J. Manuf. Process.* **2017**, *25*, 134–152.

125 Watson, G.S.; Green, D.W.; Schwarzkopf, L.; Li, X.; Cribb, B.W.; Myhra, S.; Watson, J.A. A gecko skin micro/nano structure – A low adhesion, superhydrophobic, anti-wetting, self-cleaning, biocompatible, antibacterial surface. *Acta Biomater.* **2015**, *21*, 109-122.

127 Xu, H.; Cong, W.; Yang, D.; Ma, Y.; Zhong, W.; Tan, P.; Yan, J. Microstructure and mechanical performance of dissimilar metal joints of aluminium alloy and stainless steel by cutting-assisted welding-brazing. *Int. J. Adv. Manuf.* **2022**, *119*, 4411–4421.

129 Yang, L.; Deng, Z.; He, B.; Özel, T. An Experimental Investigation on Laser Surface Texturing of AISI D2 Tool Steel using Nanosecond Fiber Laser. *Lasers Manuf. Mater. Process.* **2021**, *8*, 140–156.

134 Zhang, Y.; Nørgaard Hansen, H.; Bissacco, G.; Biondani, F. Comparison of selected processes for surface microstructuring of complex mould for an implanted device. *Int. J. Adv. Manuf.* **2018**, *97*, 2741–2748.

135 Zhao, D.; Tian, Q.; Wang, M.; Jin, Y. Study on the Hydrophobic Property of Shark-Skin-Inspired Micro-Riblets. *J. Bionic Eng.* **2014**, *11(2),* 296-302.

136 Zheng, K.; Yang, F.; Zhang, N.; Liu, Q.; Jiang, F. Study on the Cutting Performance of Micro Textured Tools on Cutting Ti-6Al-4V Titanium Alloy. *Micromachines* **2020**, *11*, 137.

138 ISO. 4287 *Geometrical Product Specifications (GPS)—Surface Texture: Profile Method—Terms, Definitions and Surface Texture Parameters*; ISO: Geneva, Switzerland, 1997.

139 ISO. 4288 *Geometrical Product Specifications (GPS)—Surface Texture: Profile Method—Rules and Procedures for the Assessment of Surface Texture*; ISO: Geneva, Switzerland, 1996.

140 https://www.atriainnovation.com/en/microstructuring-of-surfaces/, accessed in 2020.03.25

141 https://www.webofscience.com/, accessed in 2020.05.20

142 https://www.olympus-lifescience.com/en/microscopes/upright/

143 https://www.leica-microsystems.com/products/light-microscopes/p/leica-dm-il-led/

144 https://www.trumpf.com/en_INT/products/laser/marking-lasers/trumark-series-5000/

151 https://www.ossila.com/products/contact-angle-goniometer

157 https://sciencing.com/calculate-pulse-width-8618299.html

Abstract

Due to its wide applicability in industry, devising microstructures on the surface of materials can be easily implemented and automated in technological processes. Laser Surface Texturing (LST) is applied to modify the chemical composition, morphology, and roughness of surfaces (wettability), cleaning (remove contaminants), reducing internal stresses of metals (hardening, tempering), surface energy (polymers, metals), increasing the adhesion (hybrid joining, bioengineering) and decreasing the growth of pathogenic bacteria (bioengineering). The material selected for LST is ferritic stainless steel AISI 430, distinguished by the low cost in manufacturing, corrosion resistance and high strength at elevated temperature. Three different patterns (crater array type C, two ellipses at 90° overlapping with its mirror-type B and 3 concentric octagons-type A) were applied with a nanosecond pulsed laser (active medium Nd: Fiber Diode-pumped) on the surface of a ferritic stainless steel (AISI 430). Effect investigation of laser parameters of thermal affected area and micro-structures is accomplished by morphological analysis (SEM+EDS). Micro texturing the surface of a material can modify its wettability behaviour. A hydrophobic surface (contact angle greater than 90°) was obtained with different variations depending on the parameters. The parameters of the laser micro-patterning have a marked influence for the results, creating microstructures groove-type sections with different depths and recast material. Micro-texturing is essential for dissimilar materials welding, due to the formation and interlocking of grooves on the metal surface.

Rezumat

Datorită aplicabilității sale largi în industrie, conceperea microstructurilor pe suprafața materialelor poate fi ușor implementată și automatizată în procesele tehnologice. Texturarea suprafeței cu laser (LST) se aplică pentru a modifica compoziția chimică, morfologia și rugozitatea suprafețelor (umectabilitate), curățarea (înlăturarea contaminanților), reducerea tensiunilor interne metalelor (călire, revenire), energia de suprafață (polimeri, metale), creșterea aderenței (îmbinări hibride, bioinginerie) și diminuarea dezvoltării bacteriilor patogene (bioinginerie). Materialul selectat pentru LST este oțelul inoxidabil tip feritic AISI 430, care se distinge prin costul scăzut de fabricație, rezistența la coroziune și rezistența ridicată la temperatură ridicată. Trei modele diferite (crater de tip C, două elipse la 90° suprapuse în oglindă de tip B și 3 octogoane concentrice de tip A) au fost aplicate cu un laser pulsat în nanosecunde (mediu activ Nd: Fiber Diode-pompat) pe suprafața unui oțel inoxidabil feritic (AISI 430). Investigarea efectului parametrilor echipamentului laser, a micro texturilor și zonei influențate termic se realizează prin analiza morfologică (SEM+EDX). Microtexturarea suprafeței unui material poate modifica comportamentul său de umectare. S-a obținut o suprafață hidrofobă (unghi de contact mai mare de 90°) cu diferite variații în funcție de parametrii utilizați. Parametrii micro-modelului texturat cu fasciculul laser au o influență marcantă asupra rezultatelor, creându-se astfel microstructuri cu secțiuni de tip canelură având adâncimi de diferite dimensiuni și material expulzat din crevasă pe marginea acesteia. Microtexturarea este esențială pentru îmbinări hibride, datorită formării și interblocării microtexturilor create pe suprafața metalică.

PERSONAL INFORMATION

Moldovan Edit Roxana

0040 741 341 922

edit.moldovan@unitbv.ro

Sex female | Date of birth 08/10/1986 | Nationality romanian

EDUCATION AND TRAINING

2016-present
Ph.D. student
Transilvania University of Brasov, Materials Science and Engineering Faculty

2014-2016
M.Sc in Welding engineering of advanced materials
Transilvania University of Brasov, Materials Science and Engineering Faculty, Welding Engineering of advanced materials.

2010-2014
BS
Transilvania University of Brasov, Civil Engineering Faculty, Civil Engineer.

2001-2005
High School
Economic High School, High School diploma,

PERSONAL SKILLS

Mother tongue(s): Romanian

Other language(s)

	UNDERSTANDING		SPEAKING		WRITING
	Listening	Reading	Spoken interaction	Spoken production	
English	C1	C1	C1	C1	C1
Italian	C1	C1	C1	C1	B1
French	B2	B2	B2	B2	A2
Hungarian	B2	B2	B2	B2	A2

Levels: A1/2: Basic user - B1/2: Independent user – C1/2 Proficient user
Common European Framework of Reference for Languages

ADDITIONAL INFORMATION

Publications
Presentations
Projects
Conferences
Awards

3 papers in ISI journals, 1 paper in BDI journal
2 poster presentations at International Conferences
3 oral presentations at International Conferences
Prizes:

- III prize at National Scientific Session of Student Communications “CIBv2012”, *Special Concrete*, May 2012;
- Prize Section XI, at Absolvenți în Fața COmpaniilor, “AFCO 2021“;
- Best oral presentation and Best Paper Award, at ICIR Euroinvent 2022-International Conference on Innovative Research;

2 participations at National Scientific Sessions of Student Communication.
Poster presentation:

- Moldovan E., Tierean M.H., Stanciu E.M., *Overview of Joining Dissimilar Materials: Metals and Polymers*, Bulletin of the Transilvania University of Braşov, Series 1, Vol. 10 (59) No. 1 - 2017, pg. 238.
- Moldovan E., Tierean M.H., Stanciu E.M., *Overlap laser welding of thin polycarbonate sheets*, Bulletin of the Transilvania University of Braşov, Series 1, Vol. 10 (59) No. 1 - 2017, pg. 237

Awards:

- III prize at National Scientific Session of Student Communications “CIBv2012”, *Special Concrete*, May 2012;
- Prize Section XI, at Absolvenți în Fața COmpaniilor, “AFCO 2021“;
- Best oral presentation and Best Paper Award, at ICIR Euroinvent 2022-International Conference on Innovative Research;

Conferences:

- National Scientific Session of Student Communications “IAcSIc”, May 2012
- National Scientific Session of Student Communications “CIBv2012”, May 2012
- The International Anniversary Conference “CIBv”, October 2013
- The International Conference “BraMat”, 2017
- ICIR-International Conference on Innovative Research 2021;
- The International Conference “BraMat”, 2022;
- ICIR-International Conference on Innovative Research 2022;